LUND UNIVERSITY

Modelling the evolution of an ion beam through a 3 MV Pelletron accelerator

Niek van Woudenberg

Department of Physics
Division of Nuclear Physics

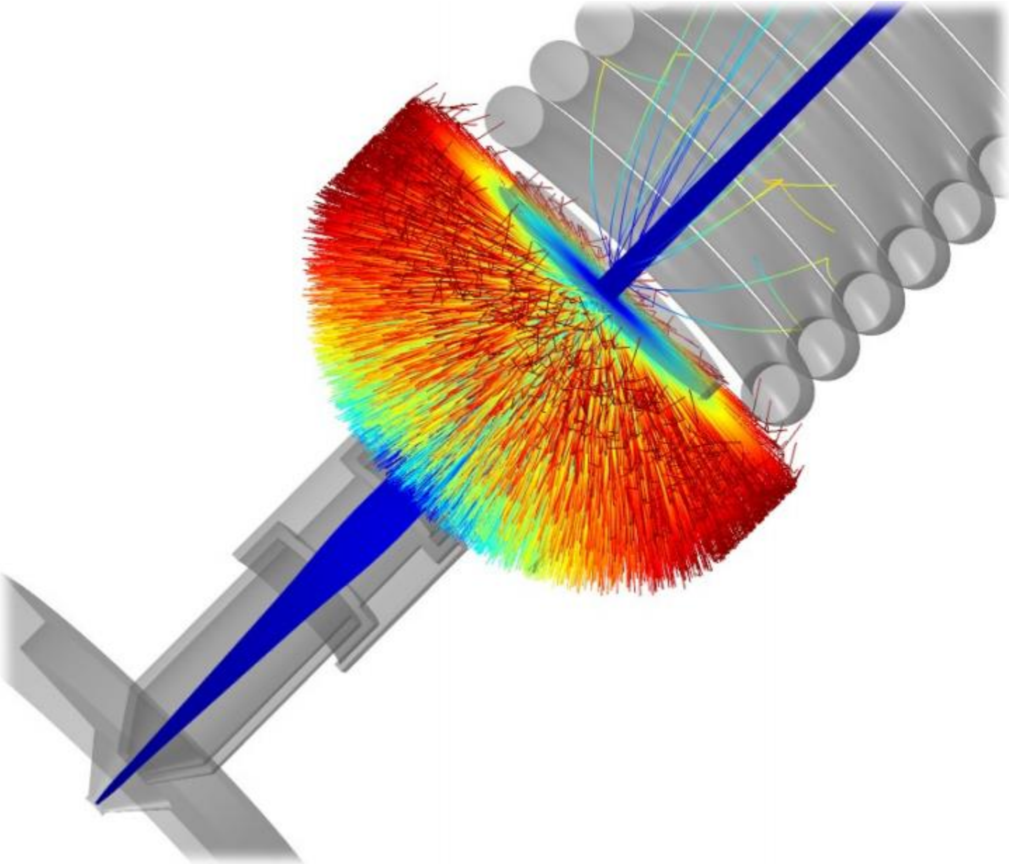

Supervisor: R.J.W. Frost (LU)
Co-Supervisor: J. Pallon (LU)
Project Coordinator: S. van Ekeren (SU)

THESIS SUBMITTED FOR THE DEGREE OF BACHELOR OF SCIENCE
AT SAXION UNIVERSITY OF APPLIED SCIENCES

SAXION UNIVERSITY OF APPLIED SCIENCES

Project Duration: 6 months

August 26, 2021

This work was carried out under the Division of Nuclear Physics of Lund University for the Bachelor Of Science degree at Saxion University Of Applied Sciences. This version of the project report includes a number of changes compared to the original submission at Saxion University of Applied Sciences. The changes are as follows:

- altered front cover,
- fixing of typographical errors,
- amended reference list.

Abstract

In this work simulations of the LIBAF Pelletron were performed to gain insight into the parameters that govern the machine operation and control. Three simulation packages: COMSOL, WARP and TURTLE/TRANSPORT were employed, and cross-validation of these software packages was performed by test-case simulations. The major components of the Pelletron were simulated on a individual basis to ensure their behaviour was well understood. These components were finally incorporated into a full source-to-exit simulation in COMSOL. Disagreement by a factor of two was found between the beam divergences predicted by TURTLE and the other two packages at an initial energy of 30 keV, for test-case simulations. Good agreement was seen in test-case simulations of the Einzel lens, for the envelopes and focal points, predicted by WARP and COMSOL. A focal point at infinity was obtained for Einzel potentials of between 12.7 and 12.8 kV, for both packages. For the full LIBAF Pelletron simulation in COMSOL, the emittance of the beam exiting the machine was found to be proportional to the beam current. This proportionality indicating that simulations of this type could potentially be used to optimise the accelerator settings for specific user needs. As beam losses were also quantified in the full Pelletron simulations, it is possible to estimate the maximum attainable beam current from the machine, for a given set of user setting, if the current produced by the ion source is known.

Contents

List of Figures

List of Tables

List of Abbreviations

APR	Aperture Pass Ratio
CERN	Conseil Européen pour la Recherche Nucléaire
COMSOL	COMSOL Multiphysics®
CPT	Charged Particle Tracing
CPU	Central Processing Unit
FDM	Finite Difference Method
FEM	Finite Element Method
GUI	Graphical User Interface
IBA	Ion Beam Analysis
KV	Kapchinskij-Vladirmiski
LIBAF	Lund Ion Beam Analysis Facility
NEC	National Electrostatics Corp
NRA	Nuclear Reaction Analysis
OS	Operation System
PDE	Partial Differential Equations
PIC	Particle In Cell
PIXE	Particle Induced X-ray Emission
PSI	Paul Scherrer Institute
RAM	Random Access Memory
RF	Radio Frequency
SE	Standard error

List of Symbols

x	x position
y	y position
z	z position
p_x	x momentum
p_y	y momentum
p_z	z momentum
Z	Atomic number
l	Path length
δ	Fractional momentum
s	Displacement along reference trajectory
α	Alpha Twiss
β	Beta Twiss
γ	Gamma Twiss
ϵ	Emittance
σ	beam matrix
σ_s	Sample standard deviation
N	Number of particles
β_r	Relativistic beta
v	Velocity
γ_r	Relativistic gamma
c	Speed of light
m	Mass
m	Rest mass
K	Generalized perveance
q	Elementary charge
I_b	Characteristic current
ϵ_0	Permittivity of free space
v_b	Beam velocity
U_p	Probe potential
U_e	Einzel potential
U_b	Bias potential
U_t	Terminal potential
U_i	Ion potential
E_f	Final energy
E_0	Initial energy
E_{rel}	Relativistic energy
E_{clas}	Classic energy
v_f	Final velocity
$\vec{E}$	Electric field

$\vec{B}$	Magnetic field
F_E	Electric force
F_B	Magnetic force
M	Matrix
d	Gap distance
f	Focal point
t	Time (variable)
T	Time (constant)
R_1	Major radii of ellipse
R_2	Minor radii of ellipse
θ	Ellipse angle
t	Time (variable)
T	Time (constant)
r	Radius
r_{12}	Correlation matrix
P	Central momentum
S	Beam species
x_i	Initial x
xp_i	Initial x'
L_d	Length drift
L_a	Length acceleration
R	Geometric radius
S_t	Section thickness
N_r	Number of rings
N_s	Number of sections
U_s	Step potential
i	Section integer

Acknowledgements

First of all I would like to show my deep and sincere gratitude to Rob Frost for his supervision and his efforts throughout this project. I have learned a great deal from him and am amazed by his involvement and dedication. In addition, I would like to thank Jan Pallon and Mikael Elfman for their support in this project and their friendliness. I would like to extend my sincere thanks to my friend Julian Koedam for providing his personal computer to run simulations and for his moral support, you're the boss! I also want to show sincere thanks to George Gillespie of G. H. Gillespie Associates Inc. for answering questions and his help. My gratitude also goes out to Thom Pollock of NEC for allowing me to use the Pelletron schematics in this report. Finally I want to thank my university supervisor Stefan van Ekeren for his guidance and support.

1 Introduction

Particle accelerators are complex machines, in which vacuum technology, high voltage, radio frequency, radiation and high energy ions all come together. The control and operation of these machines are in most cases still based on trial and improvement. Particle accelerator codes were developed to attain more knowledge about the principles involved in these machines, resulting in the design of a new generation of particle accelerators. These new generation of accelerators are able to produce higher currents, generate increased neutron flux, more events in collisions for particle physics or better resolution as nuclear microprobes. Although a wide variety of simulation codes is available and being developed, cross-validation of these accelerator codes is lacking. In Section 1.2.1 an overview is given of the project and the key project goals are stated. The facility and accelerator are introduced in section 1.2.1 and 1.2.2 respectively. In the remainder of this introductory chapter, Chapter 1.3, the structure of the report is discussed.

1.1 Project Overview and Key Project Goals

One of the goals of this work is to provide such a cross-validation with three software packages, COMSOL, TRANSPORT/TURTLE and WARP. This cross-validation is performed by running simulations with test-cases in general scenarios. These simulations will be expanded for the LIBAF accelerator at Lund University, where each component is modelled on a individual basis. The end result will be an incorporated model of the LIBAF accelerator components, resulting in a source-to-exit simulation.

The three key goals are of this work can be summarized as:

1. Comparison of the acceleration simulation codes,
2. Modelling of individual accelerator components,
3. Incorporation of individual accelerator components into a full source-to-exit simulation of the LIBAF Pelletron.

1.2 Background and Motivation

1.2.1 The Lund Ion Beam Analysis Facility (LIBAF)

At the LIBAF (Lund Ion beam Analysis Facility), extensive research is being carried out within the field of IBA (Ion Beam Analysis). The lab is pictured in figure 1.1, showing the pelletron accelerator, three beam lines and the experimental chambers at the end. The middle beam line will be used for neutron production in the near future [1, 2]. The analysis techniques used in these experimental chambers include PIXE (Particle Induced X-ray

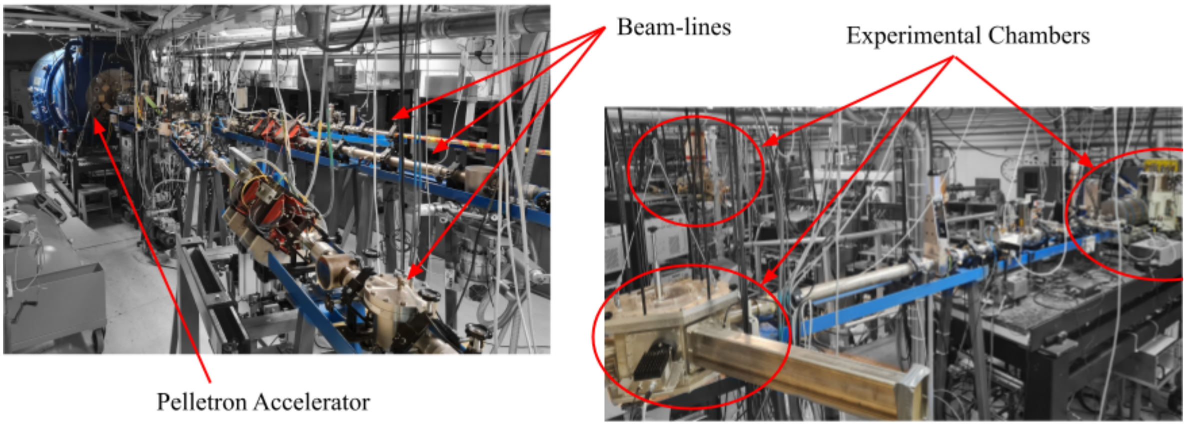

Figure 1.1: Pelletron accelerator, beam-lines and experimental chambers at the Lund Ion Beam Analysis Facility, Lund, Sweden. Courtesy of R.J.W. Frost, LIBAF [9].

Emission) [3], RBS (Rutherford Back Scattering) [4] and NRA (Nuclear Reaction Analysis) [5], all of which can be used to determine sample composition by irradiating it with an MeV ion beam. A schematic showing all the processes that can occur when irradiating a sample with an ion beam can be seen in Figure 1.2. In PIXE, the sample irradiation causes characteristic x-ray emission that can be used to quantify elements with $Z > 11$ and was developed at Lund University from 1970 to 1984 [3]. In RBS the ion beam collides with heavier elements in a sample which in turn causes back scattering of the incident ions. The scattered ions are collected and analysed to gain information about the depth profile, it is widely used within material science to determine composition or contamination of a sample [6, 7]. Another method for depth profiling is NRA, in which the targeted elements undergo nuclear reactions. From these reactions, protons, alpha particles or gamma rays are emitted which can be detected [6, 8].

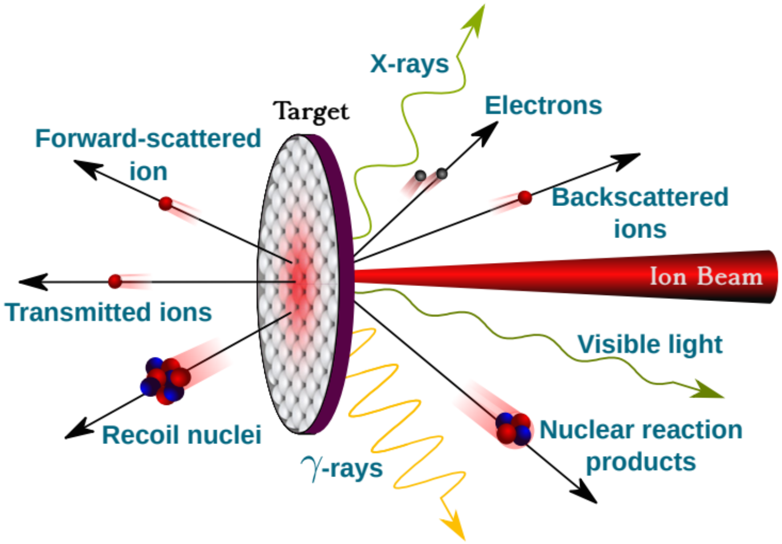

Figure 1.2: A schematic of the nuclear processes involved in IBA. Reproduced from [5] with permission of Nathaly de La Rosa.

In IBA the quality of ion beam that interacts with the sample is determinative in the analysis of the sample. It is therefore of great importance that the produced ion beam is of high quality and its operation is well understood. Three crucial parameters determine the quality; the energy, the current and the divergence of the ion beam. The energy is an important variable in this accelerator setup because it determines the cross sections of reactions in the sample. Therefore, the energy spread must be temporally and spatially stable and small in magnitude. The same applies to the current, deviation in the current results in a poor normalisation of data. Moreover, a high current might damage the sample while a low current might not produce any data at all. The divergence of the ion beam is decisive in the maximum obtainable beam current and lateral resolution as a microprobe.

1.2.2 The LIBAF Pelletron

The ion beam used at LIBAF is produced by an single ended 3 MV electrostatic accelerator from NEC (National Electrostatics Corp.), which generates a continuous ion beam [10]. A moving chain with pellets is used to charge the terminal shell in a manner similair to a Van De Graaf accelerator, as can be seen in Figure 1.3. The terminal shell can be charged up to a potential of 3 MV [11]. The positive ion source is located within the terminal shell itself and is followed by an Einzel lens, velocity selector and the acceleration column.

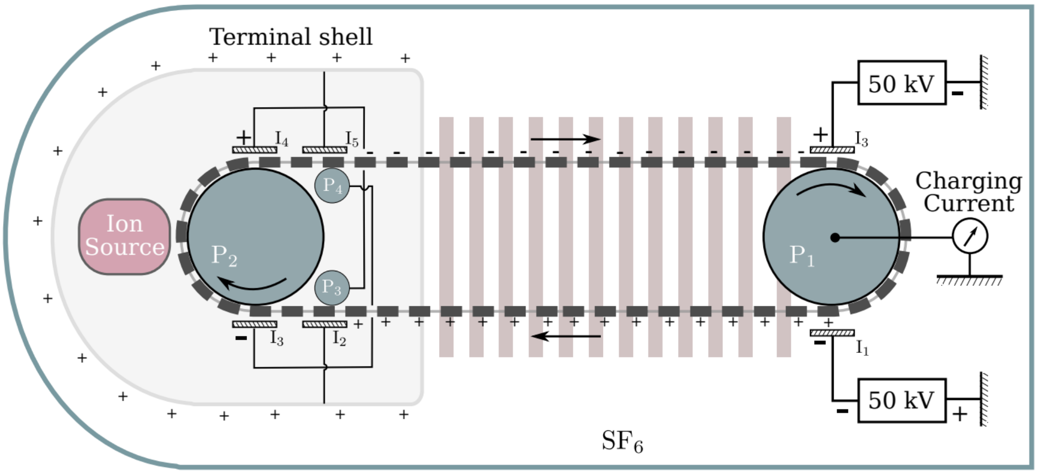

Figure 1.3: Schematic overview of the working principle of a Pelletron accelerator. Reproduced from [5] with permission from Nathaly de La Rosa.

The ion source is capable of producing proton, deuterium and helium beams with currents at the exit of the machine up to 15 µA. Ions are extracted from the gas bottle by the probe which is situated in the ion source. The Einzel lens is used to focus the beam and the velocity selector is employed to filter particles of a specific energies. In the acceleration column the beam is accelerated to the terminal energy. Two steering magnets are located at the exit of the machine to adjust the direction and position of the beam. Following the exit, the beam-line or transport line begins. To avoid sparking and making the accelerator assembly more compact, the whole system is enclosed by a pressure tank that contains SF_6 gas at a pressure of around 5 bar.

Insight into the element-parameters and how they affect the beam is lacking. Currently the beam is controlled by means of trial-and-improvement, which makes obtaining optimal beam quality a time consuming process. An improvement in knowledge can be acquired by means of simulation of the various ion optical elements within the accelerator. By incorporating these individual simulations into a full model, the accelerator can be simulated from source to exit. These simulations can in turn be used as input for the actual accelerator elements and a study on optimisation can be performed.

Optimisation of the beam taken out from the accelerator is dependent on a number of variables which are set manually by the user. It has long been desired that constraints on these variables be placed for different beam requirements e.g. energy, current and profile. To derive such constraints, and so optimise the use of this accelerator, a full simulation using a state-of-the-art beam dynamics simulation package is required, modelling the accelerator from ion source to beam-line.

1.3 Structure of this Report

Following this introductory chapter, Chapter 2 outlines the fundamental theory of transverse beam dynamics, relativistic effects and space charge. An overview of the Pelletron accelerator system and the principles that govern these accelerator components is discussed, and simulation methods are described. In Chapter 3 the modelling approach and assumptions are discussed followed by the Software/Simulation Codes, initial beam conditions and the comparison of simulation codes. At last the approach to simulation of the individual accelerator components and the full accelerator simulation is given. In Chapter 4, results of the simulated work are presented, and in Chapter 5 they are discussed. Finally, Chapter 6 present a summary of the major findings of this work and provides suggestions for future work.

2 Theory

In an electrostatic accelerator, ions are created and extracted through focusing and filtering elements before being accelerated by an acceleration structure and exiting the machine. For studying the evolution of an ion beam through an accelerator it is important that the beam dynamics are well understood. In most literature, a difference exists between the transverse dynamics and the longitudinal dynamics. Longitudinal dynamics focuses mostly on the energy of the ion beam while the transverse dynamics have an effect on the profile and divergence of the beam. For a monochromatic ion beam, with a single, energy constant for all particles, the longitudinal dynamics can be neglected [12, 13].

2.1 Background

2.1.1 Transverse Beam Dynamics

The propagation of an ion beam is described by the 6D phase space which includes all particle states derived from the equations of motion. The six dimensional phase space consists of three positional dimensions and three momentum dimensions, expressed as:

$$< x, y, z, p_x, p_y, p_z > . \tag{2.1}$$

The elegant property of the phase space is that the density of the 6D phase space is conserved under the influence of conservative forces (Liouville Theorem) and thus, the beam acts as an in-compressible liquid [14]. The phase space is often plotted as the "trace space", in which the coordinates are replaced by the prime coordinate system:

$$< x, y, z, x', y', z' >, \tag{2.2}$$

where the prime variable, also the angle or transverse and longitudinal velocity of the beam is generalized for any coordinate and defined as:

$$u' = \frac{v_u}{v_z} = \frac{du}{dt} \cdot \frac{dt}{ds} = \frac{du}{dz}, \tag{2.3}$$

in which s is the longitudinal position. In linear systems $(s = t)$. Trace space is often plotted in the transverse planes x and y and the longitudinal plane z, treating the planes independently as they are only weakly coupled [15, 16]. The trace space is used because it connects better to measurable quantities compared to the phase space. One has to keep in mind that the theorems apply only to the phase space in momentum coordinates. The state of a single particle in transverse dynamics is commonly expressed as the vector:

$$\vec{x} =< x, x', y, y', l, \delta >, \tag{2.4}$$

where l is the path length between the particle trajectory and the reference trajectory and $\delta = \frac{\Delta p}{p}$ is the fractional momentum deviation from the reference trajectory [17]. A more comprehensive way to describe the phase space and transformations of the phase space is by using matrix formalism. A single particle described by the state vector $\vec{x}(s)$ can be transformed by a matrix multiplication [15, 18]:

$$\vec{x}(s) = \mathcal{M}(s)\vec{x}(0). \tag{2.5}$$

The transformation matrix $\mathcal{M}$ represents an ion optical element or effect in the beamline (quadruples, dipoles, lenses, aberrations etc). This can be expanded for a beam by introducing the beam matrix σ which includes all the particle states in an ellipse surrounding the infinite particle distribution[15, 14]:

$$\sigma = \epsilon \begin{pmatrix} \beta & -\alpha \\ \alpha & \gamma \end{pmatrix} \tag{2.6}$$

where, α, β and γ are the Twiss parameters and ϵ the beam emittance. The Twiss parameters define the ellipse in the phase space, the ellipse for the x-dimension can be seen in Figure 2.1. Transformations of the beam matrix through a matrix system is described by the tensor transformation [19]:

$$\sigma(s_1) = \mathcal{M}(s)\sigma(s_0)\mathcal{M}^T(s). \tag{2.7}$$

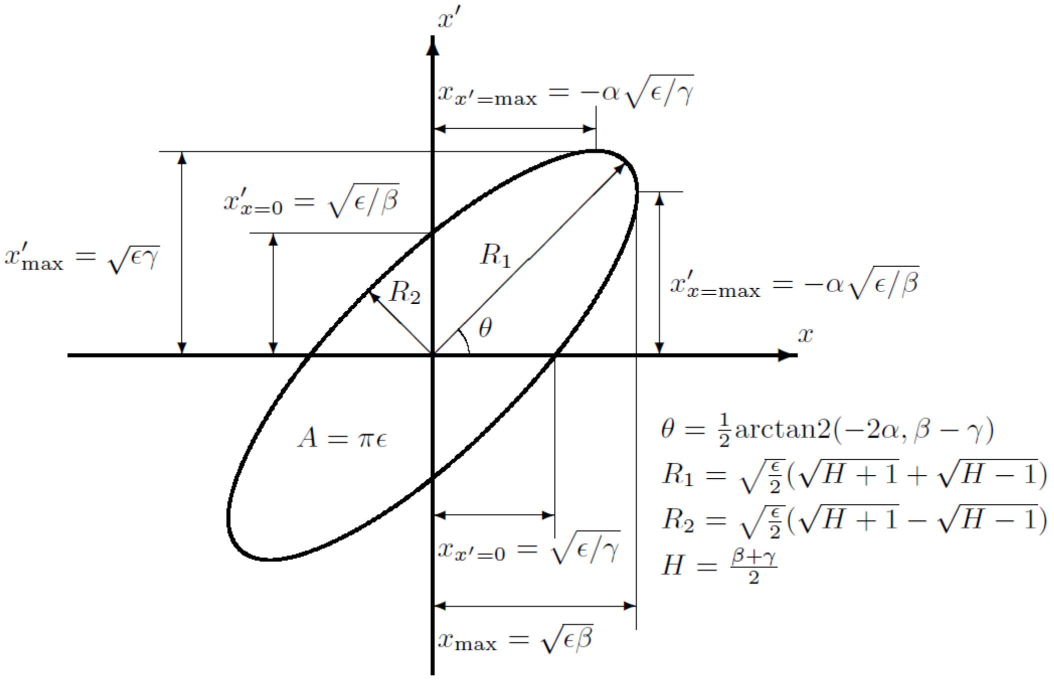

Figure 2.1: The phase space ellipse for x showing the Twiss parameters and the relation to the phase ellipse dimensions. Adapted from [15] with permission of T. Kalvas.

Matrix formalism is mostly used to solve the equations of motion up to the 5^{th} order. The matrix multiplication of elements is "hard edged", meaning that the elements do not affect each other and are inserted separately. Collective effects are generally not considered or approximated by drift matrices if the significance of space charge is known [20, 18, 21, 14].

Phase space sampling

There are various ways to sample particles from the required input phase space. The KV (Kapchinskij-Vladirmiskij) distribution is an uniform distribution in the phase space [22]. The Gaussian distribution or normal distribution is non-uniform in phase space and has a better resemblance to the actual particle distributions in particle accelerators [23]. The standard deviation of particle distribution can be calculated by:

$$\sigma_s^2 = \frac{1}{N}\sum N_b * x^2. \tag{2.8}$$

2.1.2 Relativistic Considerations

In a particle accelerator it is often necessary to consider relativistic effects because of the high velocity of the particles in an ion beam. These effects are crucial in the accelerator design and operation. The most significant effect is the transfer of energy to mass instead of velocity [12].

The relativistic effects can be expressed by the Lorentz factor:

$$\gamma_r = \frac{E}{E_0} = \frac{m}{m_0} = \frac{1}{\sqrt{1-\beta_r^2}}, \tag{2.9}$$

where E is the total energy, E_0 the rest energy, m the mass of the particle, m_0 the rest mass of the particle and β_r the relativistic beta factor given by:

$$\beta_r = \frac{v}{c} = \sqrt{1-\frac{1}{\gamma_r^2}}, \tag{2.10}$$

in which v is the velocity of the particle, γ_r the relativistic gamma factor and and c the speed of light ($3.8\mathrm{e}^8$). The need to include relativistic effects is generally accepted to be for $\beta_r > 0.1$, at which an error of 1% is induced at a proton energy of 6.3 MeV [24].

2.1.3 Space Charge

A very important aspect of the ion beam is its space charge, as the name indicates it is the charge of the beam itself confined to some space. The confined charges have the same sign (for an ideal beam) and therefore, experience coulombic repulsion. The repulsion between all the particles in the ion beam causes the beam to diverge. This is a non-linear effect causing emittance growth, halo formation and even particle loss. In addition, it also limits the maximum beam current and focusing in a particle accelerator [25]. The space charge effect is very significant for high current density beams with relatively low velocities [26]. Besides the diverging effect, there also exist space charge compensation effects. At high velocities the magnetic self field of the beam becomes large and causes a focusing effect that partially nullifies the divergence. In addition, when considering a low density background gas in case of a non-ideal vacuum, collisions within the beam tube will result in secondary electrons that neutralize the space charge. The result of this compensation can neutralize or even cause a net focusing [27]. An estimation of the significance of the space charge is described by the *generalized perveance*. In the case of non-relativistic beams ($\gamma_r \approx 1$) and charge neutralisation not considered:

$$K = \frac{qI_b}{2\pi\epsilon_0 m v_b^3}, \tag{2.11}$$

where, q is the elementary charge, m is the ion mass, v_b is the beam velocity, and ϵ_0 the permittivity of free space and I_0 the characteristic current. The paraxial beam approximation is only valid for $K << 1$ [27], and $\Delta\epsilon \propto \sqrt{K}$ [26].

2.2 Electrostatic Accelerator Components

2.2.1 Overview of an Electrostatic Accelerator

An electrostatic accelerator can be divided into three main section based on their purpose:

• Ion source:	Formation of ions from gas	1-2 kV
• Extraction:	Extraction of beam, focusing and filtering	30 kV
• Acceleration:	Major acceleration of beam	3 MV

An overview of the major components effecting beam transport can be seen in Figure 2.2.

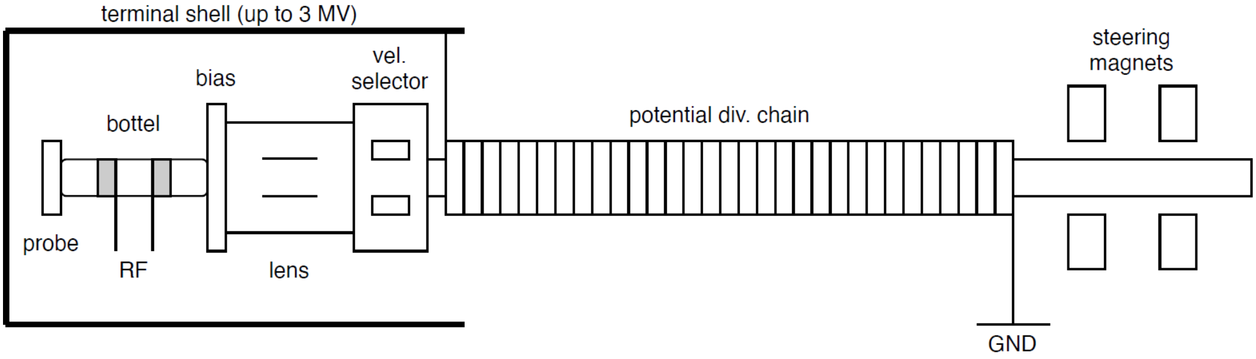

Figure 2.2: Simplified schematic of a single ended electrostatic accelerator, showing the major components responsible for beam production, shaping and acceleration. Courtesy of R.J.W. Frost, LIBAF [9].

The probe serves as an anode with potential U_p, relative to the cathode potential, U_b, of the extraction system. U_b is relative to the terminal potential U_t. As part of the extraction system the Einzel lens and Velocity selector also sit at the bias potential U_b. When considering the laboratory frame as ground, the initial potential of the ions (at rest), U_i is described by:

$$U_i = U_p + U_b + U_t. \tag{2.12}$$

2.2.2 Acceleration Column

The accelerator column is the part of the machine where major acceleration of the beam takes place. In electrostatic accelerators, acceleration takes place in a beam tube constructed of multiple rings where the potential is stepped down over by a chain of resistors. The electric field created by the potential of the acceleration column causes the particle to gain energy over the acceleration column. The final velocity can be calculated by [28]:

$$E_f = E_0 + E_{gain} = E_0 + q\Delta U. \tag{2.13}$$

The final energy at the end of an 3MV acceleration column with an initial particle energy of 30 keV is given by:

$$E_f = E_0 + \Delta E. \tag{2.14}$$

The resulting velocity of a particle in the non-relativistic case where $\gamma_r \approx 1$ velocity is given by:

$$v = \sqrt{\frac{2E}{m}}. \tag{2.15}$$

Divergence in the acceleration column will be limited because of the reduction in time that the particles spend there. This has a focusing effect on the ion beam described by the focusing of a iris doublet lens [18, 29, 30].

2.2.3 Velocity Selector

A velocity selector uses both an electric and magnetic field to filter particles based on their velocity and species. The electric and magnetic field are perpendicular to the incoming beam direction and to each other such that it results in the field orientations as shown in Figure 2.3. Particles that move too fast are deflected downwards by the magnetic force F_B and particles that move too slow are deflected upwards by the electric force F_E. The filtered velocity is determined by the electric and magnetic field ratio [31, 32].

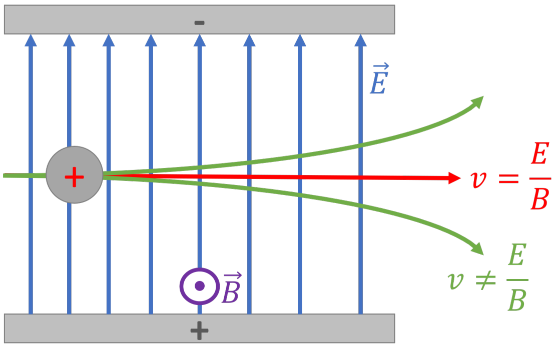

Figure 2.3: Operation principle of a velocity selector. An electric field and magnetic field are applied orthogonality to each other and to the direction of particle velocity. Particles are filtered by the electric and magnetic force, respectively F_E and F_B.

The filtered velocity is given by the fraction of the electric field and the magnetic field:

$$\vec{v}_f = \frac{\vec{E}}{\vec{B}}, \tag{2.16}$$

and filtered energy is directly related to the filtered velocity by:

$$E_f = \frac{1}{2} m v_f^2. \tag{2.17}$$

2.2.4 Einzel Lens

An Einzel lens is an electrostatic lens that is used to focus low energy ion beams by means of electric fields. It is a combination of two doublet lenses and does not change the energy of the particles. An Einzel lens exists in many geometric forms, the most common being three cylinders separated by a distance d, which can be seen in figure 2.4.

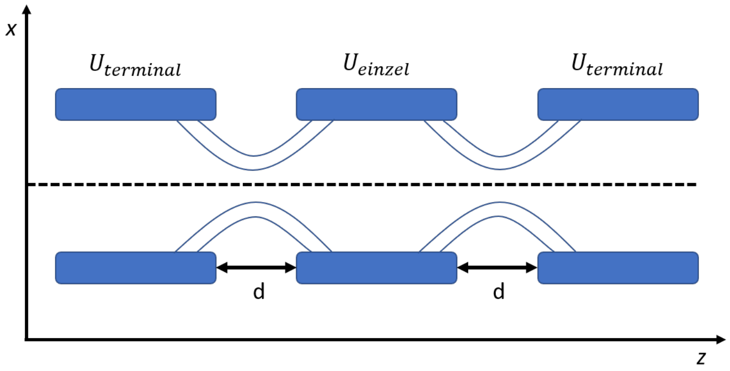

Figure 2.4: Schematic drawing of an Einzel lens with a sketch of the electric field lines.

The transformation matrix of an Einzel lens is:

$$M_{el} = \begin{pmatrix} m_{11} & m_{12} \\ m_{21} & m_{22} \end{pmatrix} = \begin{pmatrix} 4 - \frac{3R}{2} - \frac{3}{2R} & \frac{2d}{R}\frac{3R-1}{1+R} \\ \frac{3(R^2-1)(1-R)(3-R)}{8dR} & 4 - \frac{3}{2R} - \frac{3R}{2} \end{pmatrix}, \tag{2.18}$$

with R, being the focusing constant, given by:

$$R = \frac{\sqrt{U_2}}{\sqrt{U_1}} = \sqrt{1 + \frac{\Delta U}{U_1}} = \sqrt{1 + \frac{q\Delta U}{E_{kin}}}, \tag{2.19}$$

in which $\Delta U = U_2 - U_1$.

The focal length of such a lens is dependent only on the initial energy and the ratio of potentials. With a parallel input beam (pencil beam), the focal length is given by [15, 30]:

$$\frac{1}{f} = \frac{3}{8dR}(1 - R^2)(R - 1)(3 - R). \tag{2.20}$$

The focusing effect of the Einzel lens is determined by two parameters (if the distance between the gaps is considered a constant), the kinetic energy E_k and the energy of the lens $q\Delta U$. In this situation E_k is set by both the extraction energy (by probe voltage) U_p and the bias energy U_b. The energy of the lens is given by $q(U_e - U_t)$.

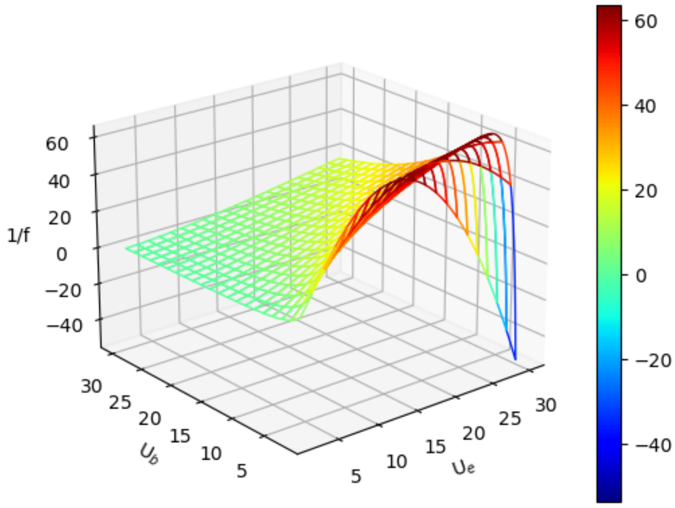

Figure 2.5: Focal length of an Einzel lens as a function of beam energy and potential difference applied between the rings at an initial energy of U_p =1.2 keV and d =5 mm.

A contour map of the parameters U_e and U_b using equations 2.19 and 2.20 can be seen in Figure 2.5. In this contour map the focal point is expressed as a function of U_e and U_b, with an initial energy of U_p =1.2 keV and d =5 mm.

2.2.5 Ion Source

The ion source is located at the start of the accelerator and is used to generate a hot plasma that is separated to create ions. These ions are extracted through an aperture and create a initial particle beam. The ion source is decisive in the main properties of the ion beam: its charge state, intensity, initial energy, shape, emittance and time structure [33].

2.3 Simulation Methods

2.3.1 Particle Approach

A distinction has to be made between single particle and multi particle models which are described as continuum. In single particle simulations the beam is represented by point particles with no internal structure or size, however, they are assigned a mass and charge. An actual ion beam consist of N particles ($N \approx 1e6 - 1e12$) and hence, if collective effects are negligible the simulation for every single particle can be executed N times. These simulations are made possible by the Liouville theorem and the corresponding phase space representation, both mentioned in Section 2.1.3. In continuum models the ion beam is not represented by a collection of particles, but rather by a continuum in the 6D phase space. In continuum simulations some collective effects of the beam are also considered and the propagation of the beam is determined by the Vlasov equation [34]. The beam propagation in a continuum is now described by the superposition of modes in frequency domain of the phase space. By using the Vlasov approach collisions between particles are not considered and fields between particles are approximated as an averaged field over the whole beam. Multi particle collective effects can be modelled in two ways, either by representing the beam as a single particle collection (large N) or by dividing the continuum space into a grid with macro particles. The former method uses the motions of particles, the latter uses evolution of the phase space [35].

2.3.2 Ray Tracing

In ray-tracing, the matrix formalism approach is used as discussed in Section 2.1.1, where the complete beam phase space is transformed as described by the σ matrix. A random generator generates the initial conditions of the particles (or rays) with a Gaussian distribution. These rays are then traced through the system of hard edged elements [36, 37, 38, 39].

2.3.3 FEM

In FEM (finite element method) the solutions to general PDE (partial differential equations) are approximated by numerical models. FEM is one of the numerical methods for finding solutions to these PDE's. The approximation to the PDE is done by means of systems of basic algebraic or polynomial equations. For a time dependent study this must be done at each time step and based on the problem linearity either basic algebraic or polynomials are used. In FEM the euclidean space is divided in multiple elements (finite element) which make up the mesh. If the mesh density is higher, then the approximation comes closer to the actual solution (this is also observed in a mesh-convergence study). The convergence is traced by an error function which is minimized to find an approximation to the PDE solution [40, 41].

2.3.4 PIC

As is stated in Section 2.3.1, for continuum models, the Vlasov equation has to be solved to determine the propagation of the ion beam. There is two ways to approach this, either with a Particle In Cell method (PIC) or by using a phase space grid method. The grid-based method is only useful in one or two dimensions since the memory usage is large, therefore, solving in 6D phase space will require extremely large memory [42]. In addition, the grid based method is prone to failure when structures that are smaller than the grid size are introduced. In contrast, PIC methods have lower memory requirements and are not sensitive to structures smaller than the grid size. In PIC a computational grid or mesh is used and the Poisson equation is solved on the grid by using the charge density distribution from the macro particles.

Initially in the PIC method a finite number of macro particles are created from a random sampling distribution in the phase space. The particles are tracked through the electric or magnetic elements and subject to these external fields as well as their self induced space charge field that is generated amongst the particles. It is commonly assumed that the self induced magnetic field is not significant for low current ion beams. The general approach of the PIC method is as follows [43, 44, 45].

0. Start with initial phase space distribution

1. Project charge densities on grid
2. Solve Maxwell's equations and combine with external fields
3. Move/Push particles (Lorentz force)
4. Repeat from (1)

There are many methods to solve Maxwell's equations, the most common are: FDM (Finite Difference Method, FEM (Finite Element Method) and Spectral methods [46, 47].

2.3.5 Meshing

The meshing and subdivision of the simulation region is a crucial aspect of numerical modelling. The mesh size has a direct influence on the simulation times and the accuracy of the model. This is very important for the final results because only geometries as small as the mesh size can be resolved. Geometry features that are smaller then the mesh size cannot be resolved and a higher quality mesh is required, smaller mesh size → longer simulation times & larger memory requirements. In addition, very sharp geometry features or small changes can have massive impact on the potentials that are calculated in the first step of the solver. An example of the artifacts caused by the mesh size can be seen in figure 4.12. The mesh size has both an effect on the field solve and on the trajectories of the particles.

3 Method

In this work simulations of the LIBAF pelletron were undertaken in three software packages: WARP, COMSOL and TRANSPORT/TURTLE. The first three sections of this chapter deal with the general aspects of the simulations and give a overview of the methods and software used. The remaining three sections detail the specifics of the simulations performed, each section addressing one of the three key project goals that are stated in Section 1.1. In Section 3.4 the methodology for comparing and contrasting the three software packages is detailed, results for which can be found in Section 4.1. The approach to the individual modelling of the major LIBAF Pelletron components is discussed in Section 3.5, with the corresponding results presented in Section 4.2. Incorporation of the independent components into a full source-to-exit simulation is detailed in Section 3.6, with results presented in Section 4.3.

3.1 Modelling Approach/Assumptions

3.1.1 Overview of Approach

There are various ways to simulate an ion beam in the chosen packages. The most straightforward package is TRANSPORT/TURTLE in which matrix formalism is used as described in Section 2.1.1. Transport uses a phase ellipse and turtle samples this phase ellipse by using ray tracing. This makes these packages somewhat inflexible and in TURTLE the only sampling possible is Gaussian. It is common to first run the Transport simulations for an approximation and use the same input file for TURTLE to do the ray tracing. In WARP there exists several ways to simulate ion beams, the methods used here are based on the lattice solver (hard-edge model) and the 3D PIC model. The lattice solver is a useful fast model solver to approximate a lattice. The 3D PIC model can solve fields within complex geometries. In COMSOL a lattice solver is not available so the FEM method was used with hard edged fields, expressed as particle forces.

Simple lattice simulations were set up to get a first approximation of the results of the lattice solvers and to cross validate the software. Simulations were run at a selection of currents, to verify that excluding space charge effects were justified. 3D simulations were implemented, in which the actual geometry of each component was taken into account. These geometries were approximated from NEC schematics with assumptions made where only incomplete schematics were available. Implementing detailed and specific geometries was further challenged by limited access to the machine. The geometries were constructed in such a way that adjusting the dimensions would be easy to implement if additional information became available. Each component was simulated independently before combining them. Simulation codes were initially compared by constructing a basic geometry in the software, involving a 0.5 m drift and 0.5 m acceleration region. Different simulation methods (lattice & 3D) were used to distinguish accuracy of these methods.

3.1.2 Major Physics Assumptions

Monochromatic Beam

In the simulations performed it is assumed that the beam has no energy spread, and is therefore monochromatic. Mono-energetic beams are practically not realistic.

Relativistic Effects

As discussed in Section 2.1.2, relativistic effects can be ignored for $\beta_r < 0.1$. For protons at the highest energy of 3 MeV in the LIBAF Pelletron, the relativistic beta factor is 0.08. By solving:

$$\frac{E_{rel} - E_{clas}}{E_{rel}} = \frac{(\gamma_r - 1)m_0c^2 - 0.5m_0v^2}{(\gamma_r - 1)m_0c^2} < 0.01, \tag{3.1}$$

for γ_r, the 1% error margin is found to be 6.3 MeV. This is more than twice the highest particle energy for protons in the LIBAF Pelletron.

Gravitational Effects

To get an estimate of the gravitational effects, a small calculation can be performed to justify exclusion from the simulations. In the machine that is approximately 3.5 m long, the particle's time of flight is 1.46 μs which corresponds to a drop of 10.5 pm. This concludes that gravitational effects were not significant and therefore ignored.

Collective Effects

Particle-particle interactions, nuclear interactions and the generation of secondary electrons were not taken into account. These were not considered because they would have introduced unnecessary complexities in the simulations that have very little influence on the overall beam evolution.

Perfect Vacuum

In all simulations the beam was assumed to propagate through a ideal vacuum, this being physically unrealistic. The pressure measured at the exit to the accelerator is $5e-9$ mbar, at which the effects of beam interaction with gas in the column is expected to be minimal. It is however, anticipated that beam broadening does occur and this is not accounted for in this work.

3.1.3 Boundary Conditions

Electrostatics

In WARP the Neumann boundary condition was used [48] for the electrostatics. The Neumann boundary condition causes the normal derivatives at the edges to be zero. In COMSOL the boundary was set by defining a terminal shell in the form of a cylinder. Thus, the electric field lines terminated on the terminal shell or boundary surface. In TURTLE and TRANSPORT, there were no numerical boundary conditions because only lattice elements are solved for.

Particle Tracing

For the particle boundary conditions in WARP, the geometry boundaries were ignored and the particles disappeared at the surrounding boundary. In COMSOL, the boundary condition for CPT in this module was set to freeze on impact, which made the particles stick to the walls when they collided with the boundaries [49]. In TRANSPORT and TURTLE, the boundary condition was set by a user defined range to calculate the ray traces.

3.1.4 Hardware

The simulations were run on both a desktop computer and a laptop computer both with Windows 10 installed. The specifications of each are shown in Table 3.1. The Laptop was used to run only a selection of the simulations in COMSOL and TRANSPORT/TURTLE. WARP was run only on the desktop computer on a virtual machine with Ubuntu 20.04.2 LTS installed. Limitations imposed by system performance, are discussed in Section 4.2.1.

Table 3.1: Hardware used for the simulations.

	DESKTOP	**LAPTOP**
OS	W10P + VM (Linux)	W10H
CPU	AMD Ryzen 5 2600	Intel i5-6200U 2.3GHz
Cores/Threads	6/12	2/8
GPU	NVIDIA GeForce GTX 970	Intel HD Graphics 520
RAM	16 GB	8 GB

3.2 Software/Simulation Codes

3.2.1 COMSOL Multiphysics®

COMSOL [50] is a standalone multiphysics simulation package. It uses the FEM [51] to model complex geometries and physical processes. The magnetic and electric fields generated by the scalar and vector potentials are modelled with the electrostatics study, within the AC/DC module or by defining the forces implicitly. To simulate the particle propagation through the electric and/or magnetic fields and geometries, the CPT (Charged Particle Tracing) [49] module was used. The sampling of the phase space can be set by the user to be: Gaussian, KV, waterbag or parabolic. In COMSOL the amount of particles per release is set and the current at which the particles are released, in this case the charge and current density are constant. A multiphysics coupling mode can couple the electrostatics and particle tracing to include collective effects like space charge. In this case the bidirectionally time depend study is used to obtain a self-consistent solution. There are nine mesh granularities available in COMSOL, defined as: extremely coarse, extra coarse, coarser, coarse, normal, fine, finer, extra fine, extremely fine.

3.2.2 TRANSPORT & TURTLE

TRANSPORT is a package originally developed at CERN [21] and modified by Urs C. Rohrer at PSI (Paul Scherrer Institute) [52]. TRANSPORT is built on a FORTRAN-77 framework with a C++ GUI (Graphic User Interface) in which the simulations are run. In TRANSPORT, matrix formalism is used and the equations of motion are solved by applying Taylor Series up to the third order. Transport is accurate within the boundary of paraxial approximation.

The simulation can be extended by using the input files of TRANSPORT in TURTLE. TURTLE is another simulation package also originally developed at CERN [39] and modified by Urs Rohrer [38]. In TURTLE, ray tracing is used in where the phase space is sampled with a gaussian distribution. In the ray-tracing method aberrations are resolved up to the 3^{th} order, also cumulative effects of higher order are included [37]. The simulation region is constructed from different lattice elements which are solved for independently by using the output of the previous element and therefore the simulations are hard-edged [52].

3.2.3 WARP

WARP is a full 3D PIC simulation kit which is open source and developed by Dave Grote and others at Berkeley lab [53, 54]. It is an advanced plasma simulation toolkit, built on a FORTRAN-77 back-end with a Python 3 front-end. One method of simulation of beam-lines and accelerators is by using a lattice description of the elements. Another is by defining the element geometries in a 3D model, these geometries are split in cells that make up the simulation grid. With the PIC model, the beam is made up of a relatively small number of particles which interact via their space-charge. The effects of the space-charge is included by a global solution of Poisson's equation, giving the electrostatic potential, at each time-step. The particle calculation can follow the time-dependent evolution of beams [55]. The particles can either be loaded onto the mesh or injected at each time step. The sampling of the phase space can be semi-Gaussian, Gaussian, parabolic, KV and waterbag, In WARP, the mesh is determined by the number of grid cells in each dimension which are user defined. The charge density and external fields are projected onto these grid cells.

3.2.4 Data Extraction

Phase Space

The phase spaces were extracted for WARP, COMSOL and TURTLE at the beginning and the end of each component modelled. The initial phase space was extracted to confirm that the input was the same for all packages and to estimate errors in the end-results due to the random sampling. The final phase space was extracted to compare the simulation codes to each other in a quantitative and qualitative way. All results were exported from the packages in ASCII format.

In WARP the phase space was extracted by taking a finite amount of particles in a volume set by the user. The fact that a volume had to be specified created uncertainty in the z-location, however, a smaller volume captured less particles and thus created larger uncertainties in the resulting phase plot. The x and x' were extracted for all particles and saved within the boundaries set by the user. In COMSOL the x and x' of all the particles at time-step t=T were extracted by writing the derived values to a table. This data was then saved to two separate files. The phase spaces were not extracted for the TRANSPORT simulations. In TURTLE the phase space data was extracted using histogram elements which saved the particles x and x' at the locations in the lattice where the elements were placed.

Emittance

ϵ was calculated by fitting an ellipse to the phase space data. For KV beams, the ellipse was simply defined as the area enclosed by the particles. For Gaussian beams ϵ was defined as one standard deviation (σ_s) of the 2D distribution in x, x'. From this the minor-, major-radii $[R_1\&R_2]$ and the angle $[\theta]$ were extracted and ϵ calculated.

Envelopes Lattice

For the lattice solver in WARP, the envelopes are extracted as a function of z and written directly to output files in ASCII format.

For a KV beam in COMSOL the envelopes are extracted by directly exporting the maximum and minimum x of the particles as a function of z. Due to symmetry in the x and y planes it was not necessary to also extract the y minima and maxima. That data was exported from a table in COMSOL, in ASCII format.

For the lattice simulations in TRANSPORT the envelopes were extracted by the σ matrices at the initial and final locations in the lattice.

Envelope Gaussian

The transverse symmetry of the beam can be exploited to obtain the $1\sigma_s$ envelope by extracting $r^2 = x^2 + y^2$ for each particle as a function of z. By further exploiting the fact that the mean of the transverse particle distribution is 0 in both x and y, extraction of $r^2(z)$ for all particles allows for the calculation of the envelope according to:

$$\sigma(z) = \sqrt{\frac{\sum_{i=1}^{N} r_i^2(z)}{N}}, \tag{3.2}$$

this holding under the condition that N is large. The uncertainty of the envelope is taken to be the standard error of the sum given by:

$$SE = \frac{\sigma_s}{\sqrt{2N}}. \tag{3.3}$$

For COMSOL and WARP, $r^2(z)$ is extracted for all particles directly in ASCII format. In TURTLE the data is extracted as histograms of r at certain locations in the lattice by the histogram elements in ASCII format.

3.3 Initial Beam Conditions

3.3.1 Parameter Matching

The three software packages each use a different method for establishing the initial conditions of the beam. The phase space of the beam is defined by the Twiss parameters (α and β) and ϵ (see Section 2.1.1). In COMSOL α and β were entered directly, and the conversion used for ϵ was:

$$\epsilon_c = \frac{1}{4} \cdot \epsilon. \tag{3.4}$$

In WARP, ϵ was entered directly and the following two input parameters, defined in terms of α and β:

$$x_{max} = \sqrt{\epsilon \cdot \beta}, \tag{3.5}$$

$$x'_{x=max} = -\alpha \cdot \sqrt{\frac{\epsilon}{\beta}}. \tag{3.6}$$

In TURTLE the following three input parameters were defined in terms of α β and ϵ:

$$x_{max} = \sqrt{\epsilon \cdot \beta}, \tag{3.7}$$

$$x'_{max} = \sqrt{\frac{\epsilon(1+\alpha^2)}{\beta}}, \tag{3.8}$$

$$r_{12} = -\frac{\alpha}{\sqrt{1+\alpha^2}}, \tag{3.9}$$

where r_{12} is the correlation matrix element (type code 12.0) to define the tilt of the beam.

The initial beam energy was directly set in WARP and COMSOL in V and keV, respectively. For single charged state particles the relation between these values is 1:1. In TRANSPORT the initial beam energy is set by the central momentum P, in units, GeV/c. The relation between the central momentum in GeV/c and the energy in keV is:

$$P = \sqrt{2m_pE}, \tag{3.10}$$

where the proton mass is 938 MeV/c^2 and E given in MeV. This conversion is only valid in the non-relativistic case, this assumption holding in the current study as discussed in Section 3.1.2.

3.3.2 Test Beam

A test beam was created to extract the initial responses of the software, this being based on physically representative parameters that are described in Table 3.2. TURTLE does not have the capabilities to generate KV beams and therefore, the sampling of the beam is either KV or Gaussian, based on the comparison with, TRANSPORT or TURTLE, respectively.

Table 3.2: Parameters describing the initial conditions of the test beam.

Parameter	**Preset**	**Descriptor**	**Relation/Assumption**
S	Proton (+)	Beam species	Used species
α	0.6	α Twiss	-
β	50 mm	β Twiss	-
ϵ	200 µm	Emittance	-
I_b	20 µA	Beam current	High threshold current
x_i	3.1623 mm	Initial x-spread	$\sqrt{\epsilon\beta}$
xp_i	73.7564 mrad	Inital x-divergence	$-\alpha \cdot \sqrt{\frac{\epsilon(1+\alpha^2)}{\beta}}$
E_{kin}	30 kV	Initial kinetic energy	Extraction from vel. sel.

3.3.3 Ion Source Output Beam

The ion source is modelled by specifications provided by NEC [56]. ϵ is defined as a function of the initial beam energy which is controlled by the probe potential according to:

$$\epsilon = \frac{4e-6}{\sqrt{U_{probe}1e-6}}. \tag{3.11}$$

For extraction by the probe with a potential of 1.5 kV, ϵ becomes $0.103 \times e - 3$ m. This is the RMS-emittance which is approximately the $1\sigma_s$-emittance at high particle ($N >> 100$). In the specification sheets a measure of the x and y maximums are given by the extraction aperture dimensions. The aperture is circular with a diameter of 1 mm. The rotation of the beam is considered to be $\theta = 0$ or "upright" and β is therefore defined as a function of ϵ and the aperture dimensions by:

$$\beta = \frac{x_i^2}{\epsilon}. \tag{3.12}$$

3.4 Comparison of Simulation Codes

3.4.1 Beam Input

To ensure an identical input for each of the simulations, the beam input was compared for the different simulation packages. For each software package the Gaussian test beam was used, described in Section 3.3.2, and the initial phase spaces were compared. This also allowed for checking that the input conversion was successful for each package. In WARP and COMSOL 10e3 particles were used, 1e4 rays were used in TURTLE.

3.4.2 Drift and Acceleration Geometry

To compare the packages a proof of concept simulation was created with a 0.5 m drift and 0.5 m acceleration region. This allowed for comparison of the packages in a concise and simple manner. Comparisons were performed with both the lattice- and 3D geometry-solver. Schematic representations of these simulation geometries are presented in Figure 3.1.

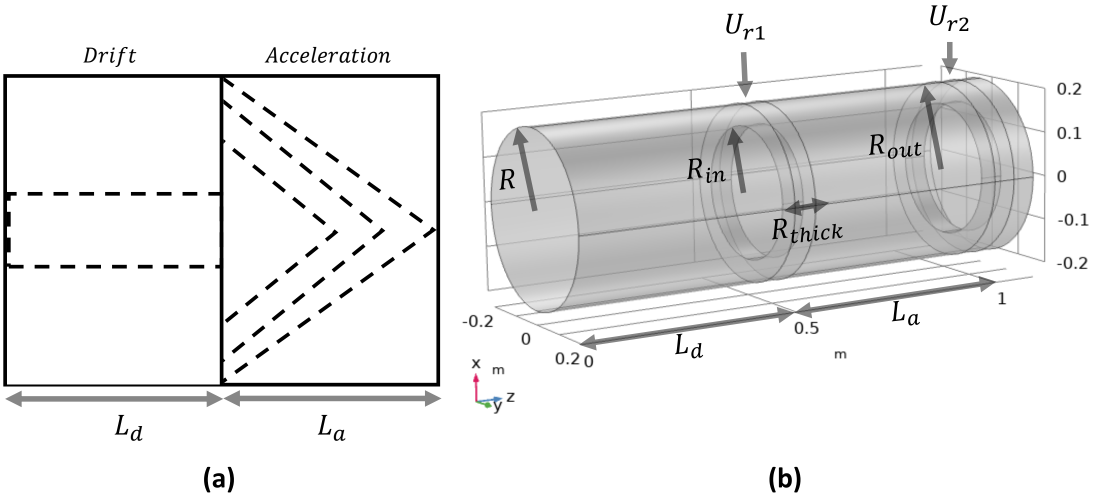

Figure 3.1: (a) A schematic representation of the lattice used in the simulations in TRANSPORT/TURTLE. (b) Geometry created in COMSOL for the simulations; The rings to which the potential is applied can be seen at 0.5 meter and 1 meter.

3.4.3 Lattice

A study on the variations in the envelopes and phase spaces, between packages, was performed. This study uses the envelope solver in TRANSPORT, both envelope solver and PIC in WARP, and CPT in COMSOL. Simulations were defined as presented in Figure 3.1(a). A detailed description of the geometry and parameters of the simulations can be found in Table 3.3.

As is discussed in Section 2.1.1, TRANSPORT and TURTLE both work with a lattice definition to run the simulation of the ion beam. In WARP the same lattice was set-up and solved with the envelope solver. PIC was used on the same lattice to generate phase space plots. The KV sampled test beam was used, as described in Section 3.3.2, with 10e3 particles. In COMSOL the effect of the lattice was approximated by using hard edged electric fields. The same test beam was used as in WARP.

Table 3.3: Parameters used in the lattice simulation. The descriptor "Tube Radius" is not used in TRANSPORT/TURTLE.

Parameter	Preset	Descriptor	Relation/Assumption
L_d	0.5 m	Drift length	-
L_a	0.5 m	Acceleration length	-
R	0.15 m	Tube radius	Boundary of simulation region
$\vec{E}_{accl}$	1.25 MV/m	Electric field strength	Comparable to column field

3.4.4 3D Geometry

To compare the three packages when propagating a beam through a defined geometry, simulations were constructed consistent with the schematic presented in Figure 3.1(b). Parameters used for these simulations can be found in Table 3.4. Beam envelopes and phase spaces are compared in the same manner as in Section 3.4.3.

As TURTLE does not have the capabilities to run 3D simulations, lattice elements were used in this package. In both WARP and COMSOL two rings with an applied potential difference were created. For all simulations the Gaussian sampled test beam was used, described in Section 3.3.2. For WARP and COMSOL 1e3 particles were used and for TURTLE 1e4 rays. For WARP the number of cells used was 64|64|256, for COMSOL the extremely fine mesh was used.

Table 3.4: Parameters used for the 3D simulation in WARP and COMSOL.

Parameter	**Preset**	**Descriptor**	**Relation/Assumption**
L_d	0.5 m	Drift Length	-
L_a	0.5 m	Acceleration Length	-
R	0.20 m	Tube Radius	Boundary of simulation region
R_i	0.15 m	Inner ring radius	-
R_o	0.20 m	Outer ring radius	-
R_t	0.05 m	Ring Thickness	-
U_{r1}	0.5 MV	First ring potential	From E-field in column
U_{r2}	0 MV	Second ring potential	Ground ring

3.4.5 Beam Energy Study

TURTLE and TRANSPORT were developed for high energy applications like those at CERN and PSI. The LIBAF Pelletron can accelerate particle to a maximum of 3 MeV and therefore, it was unknown if the software performs the same at different energies, a beam energy dependence study was conducted to identify discrepancies between the packages. The same 3D geometry that is discussed in Section 3.4.4 was used and simulated for the range of energies: [30, 50, 75, 100, 120, 150, 200, 300, 600, 1200, 2400, 4800] kV. The divergence and focal point were studied as a function of energy. The test beam discussed in Section 3.3.2 was used with a Gaussian sampling. 1e4 particles were traced through the system in WARP and COMSOL, 1e5 rays were used in TURTLE. For WARP the number of cells used was 64|64|256, for COMSOL the extremely fine mesh was used.

3.4.6 Space Charge Study

To justify excluding space charge from the accelerator modelling, a study was conducted to observe the effect of space charge at different beam currents for an initial proton beam with E_0 =30 keV. Simulations were run for a 1 m drift at eight different beam currents ranging from 1 mA to 160 mA, K=12.5e-3 to K=2e-6 respectively for 1e4 particles. The study was performed with a KV sampled test beam, see Section 3.3.2, in COMSOL only, using the bidirectionally coupled method [49] and independent particle method, for an extremely fine mesh.

3.5 Simulation of Accelerator Components

3.5.1 Acceleration Column & Mesh Convergence

Acceleration Column

A smooth and uniform electric field for the acceleration is created by approximately 20 small rings in six sections, separated by five large rings, mounted inside a ceramic beam tube. An external view of the acceleration column including ion source, Einzel lens and velocity selector can be seen in Figure 3.2. The rings shown in Figure 3.2 are for connecting the resistor chain to step down the potential, from U_t at the velocity selector exit, to ground at the accelerator exit. Each of these external rings is connected to a corresponding internal ring separated by the ceramic tube that extends over the whole acceleration column.

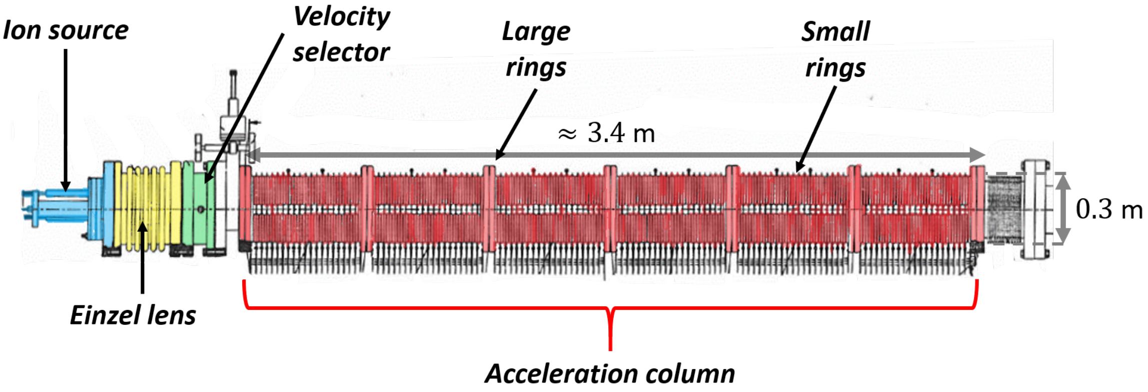

Figure 3.2: An external view of the ion source, Einzel lens, velocity selector and acceleration column. The small external rings are shown in the figure, the corresponding internal rings and the ceramic beam tube are not shown here. Six sections of 20 rings each are separated by large rings. Adapted from [57] with permission from NEC.

As no information was available on the geometry of the internal rings they were omitted from the geometries developed in WARP and COMSOL. In these simulations the external rings provided the accelerating electric field. It was assumed that despite the increased radius of the rings relative to the internal rings, the electric fields in the column would remain linear. The parameters for the geometry are summarized in Table 3.5. The geometry that was built in COMSOL can be seen in Figure 3.3. As seen in Figure 3.3 the acceleration column can be subdivided into six sections with 20 rings each. The rings were constructed in both packages by defining an array of tori.

In COMSOL, the stepped down potential was applied to the boundaries of the rings using:

$$U_{r,i}(z) = U_t - U_s \left\lfloor \frac{z - (i-1)S_t - (i-1)R_s}{R_s + R_t} \right\rfloor , \tag{3.13}$$

where $U_{r,i}(z)$ is the potential at location z in the i^{th} section, U_s the potential step per-ring, S_t the large ring thickness and R_s the separation between the rings. The large rings, seen in Figure 3.3, separating each section, were at the same potential as the last ring of the previous section and were defined by the equation:

Table 3.5: Parameters of the acceleration column.

Parameter	Preset	Descriptor	Relation/Assumption
L	3.374 m	Total length	From dimensions
R_r	15 cm	Ring radius	Approximated from drawings
R_t	2.5 cm	Ring thickness	Approximated from drawings
R_s	0.1 cm	Ring separation	Arbitrary separation
S_t	5 cm	Section thickness	$2 \cdot R_{ring}$
N_r	120	# of rings	Approximated from drawings
N_s	20	# of rings per section	Approximated from drawings
U_t	2.5 MV	Terminal potential	Nominal terminal potential
U_s	20.833 kV	Step potential per ring	U_t/N_r

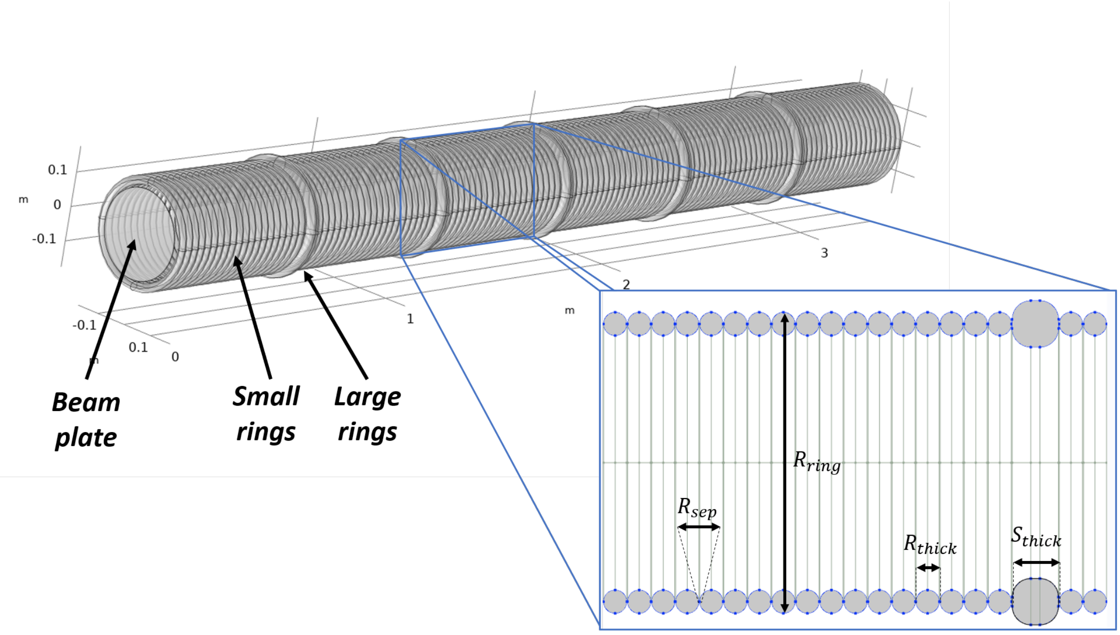

Figure 3.3: An overview of the acceleration column geometry, created in COMSOL.

$$U_{s,i} = U_0 - (i)N_s \cdot U_s, \tag{3.14}$$

where $U_{s,i}$ is the potential applied to section ring i and N_s is the amount of rings per section. In COMSOL the beam starts from a plate at the start of the column, a total of 10e4 particles were traced.

In WARP, a similar procedure for applying potentials to the geometry was used to COMSOL, however, in this case potentials were applied directly to each ring at its creation. A constant current injection was used with 1e4 particles at each time step from a virtual plate. In TURTLE the acceleration column is constructed from 120 separate acceleration elements (type code 11). After each acceleration element a histogram element (type code 50.0) is placed for data extraction. The beam is characterized by a 1.0 type element and a total of 1e5 rays were passed through the lattice. A Gaussian sampled ion source output beam was used, as described in Section 3.3.3, for all packages.

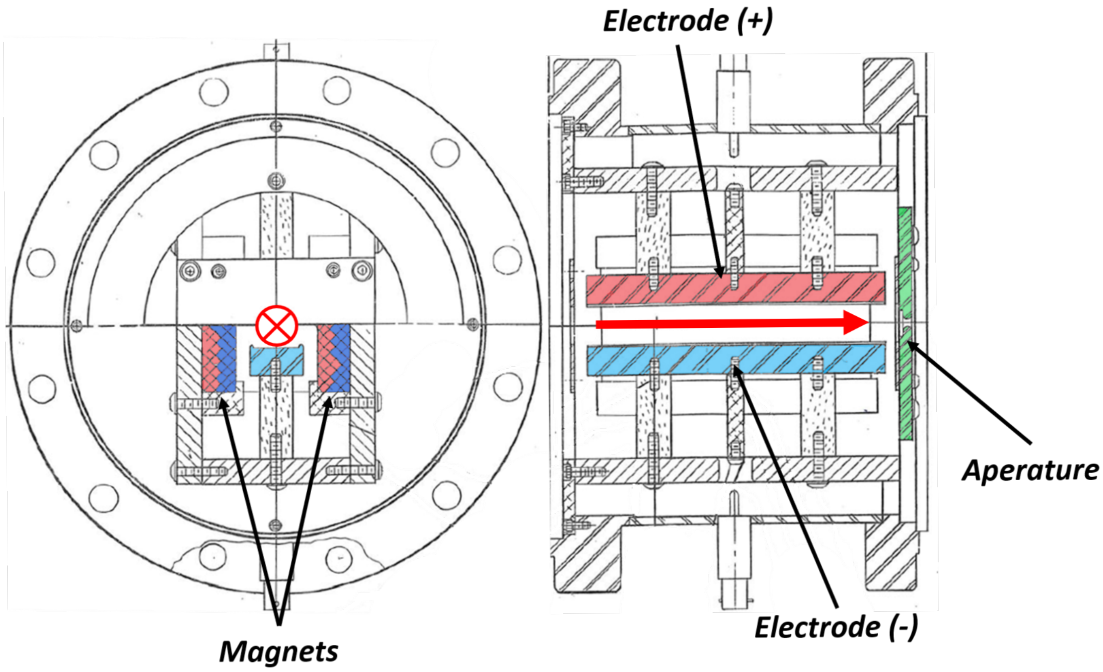

Figure 3.4: Schematic cross section and side view of the velocity selector that is installed in the LIBAF Pelletron. Adapted from [57] with permission from NEC.

Mesh Convergence Study

For the 3D simulations of the accelerator column mesh convergence was performed. The purpose of this study was to asses the changes in phase space and beam envelopes resulting from simulation using different meshes, and to find a balance between mesh size and run time. As TURTLE is not a numerical program using a mesh, it is not included in the mesh convergence study. In COMSOL, mesh granularities of: normal, fine, finer and extra fine were used in this study, see Section 3.2.1. In WARP, four different granularities of cell division were defined, these being: 50|50|75, 100|100|150, 200|200|300 and 400|400|600, cell elements in $x|y|z$.

3.5.2 Velocity Selector

A schematic of the velocity selector in the LIBAF Pelletron is provided in Figure 3.4. As the beam input utilized in these simulations is monochromatic, the beam will still be near-monochromatic when passing through the velocity selector. As such, the effects of the velocity selector are expected to be limited when electric and magnetic fields are set appropriately (see Section 2.2.3). Consequently it was decided that modelling the exact geometry seen in Figure 3.4 was not necessary and the magnetic and electric field were included as particle forces in COMSOL. The parameters used for the simulation are given in Table 3.6. Two proof of principle simulations were performed with a KV sampled ion source output beam, one with a pencil beam at an initial energy of 50 keV and another with the input from the ion source, as described in Section 3.3.3 but also with its initial energy altered to 50 keV. The number of particles used in each simulation was 1e4 with an extremely fine mesh. No simulations were performed for the velocity selector in either WARP or TURTLE.

Table 3.6: Parameters used in the simulation of the velocity selector.

Parameter	Preset	Descriptor	Relation/Assumption
L	10 cm	VS length	-
R_{tube}	15 cm	Tube radius	-
B_y	0.005 T	Magnetic flux density	-
E_{in}	50 keV	Entry energy	-
E_{filter}	50|100 keV	Filter energy	Filter off|filter on (2E)
$\vec{E}_x$	$v_{filter}B_y$	Electric field	From ratio $v = \frac{E}{B}$
v_{filter}	$\sqrt{2E_{filter}/m_p}$	Filter velocity	From $\frac{1}{2}mv^2$

3.5.3 Ion Source Extraction and Einzel Lens

Due to the complexity of plasma generation in the ion source, it was not modelled in detail in this study. The ion source output was instead defined according to the specifications provided by NEC [56] at the ion source exit, as described in Section 3.3.3 using Gaussian sampling. The extraction electrode of the ion source, seen on the right of Figure 3.5(a), was modelled as part of the Einzel lens. A schematic representation of the Einzel lens can be seen in Figure 3.5(b).

This Einzel lens in the LIBAF Pelletron consists of three electrodes placed consecutively, a potential is applied to the middle electrode U_e whereas the outer electrodes are at U_t, see in Figure 3.6. The extraction electrode is set at the potential U_b. The geometry was recreated in COMSOL and WARP by using a 2D plane, rotated around the z-axis. The simulated geometry is consistent with that shown in Figure 3.6. The collimator shown in Figure 3.5(b) was not included in the simulation. No simulations were performed in TURTLE. The phase spaces and envelopes were extracted for values of U_e ranging from 10 kV to 20 kV while

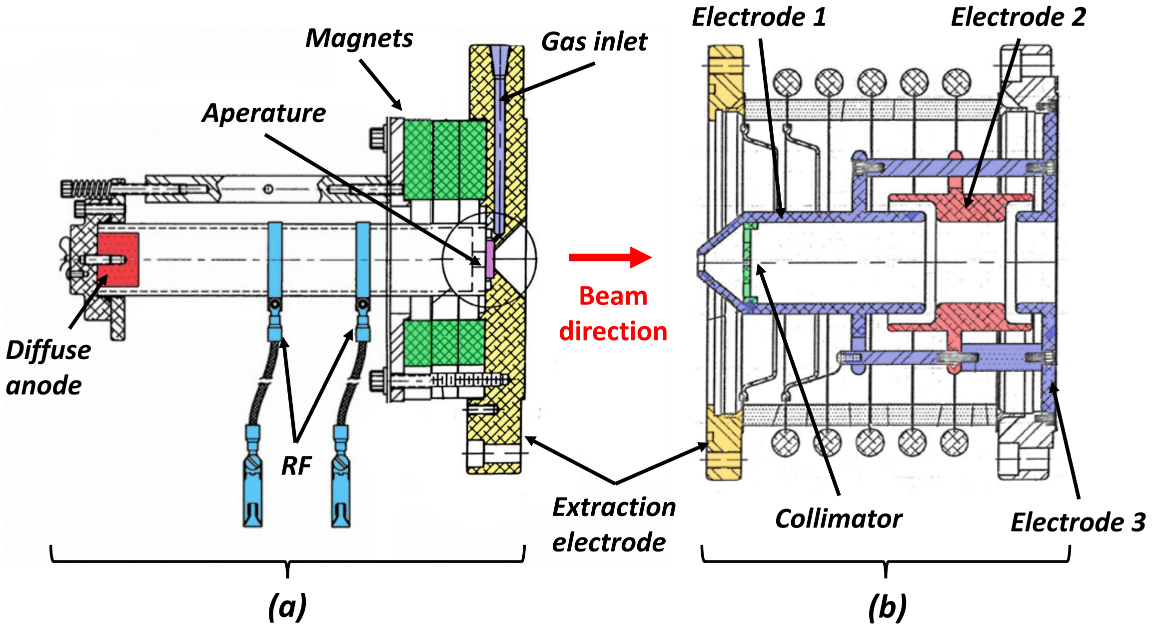

Figure 3.5: (a) Schematic representation of the ion source in the LIBAF Pelletron, adapted from [56] with permission from NEC. (b) Schematic representation of the Einzel lens in the LIBAF pelletron, adapted from [57] with permission from NEC.

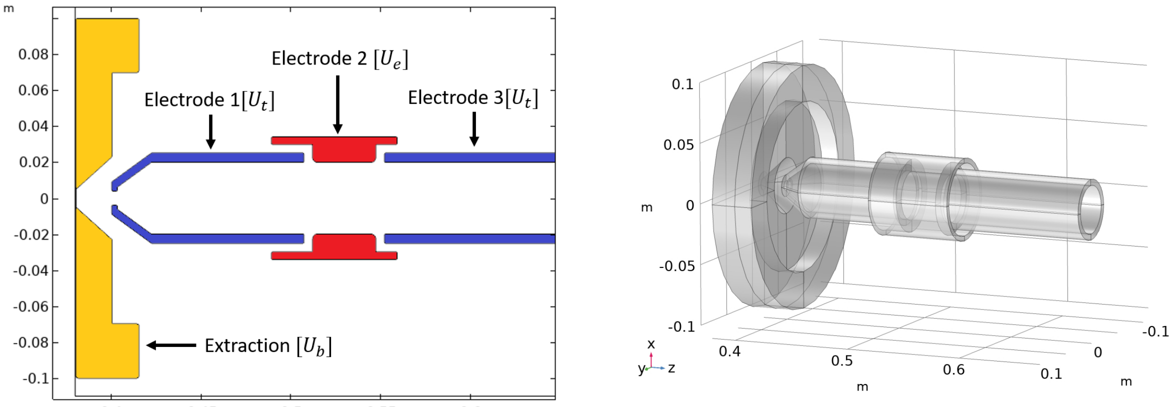

(a) **(b)**

Figure 3.6: (a) Schematic of the Einzel lens geometry used in both COMSOL and WARP. (b) Geometry created in COMSOL for the Einzel lens.

holding U_b constant. The envelopes were further used to extract the focal points. The simulations were run in WARP with a cell count of 200|200|300 and 1e3 particles, and in COMSOL with an extremely fine mesh and 1e4 particles.

3.6 Full Accelerator Simulation

A fully incorporated simulation was built in COMSOL taking into account the components that are modelled on a individual basis. The full simulation consists of the ion source output and Einzel lens discussed in Section 3.5.3, the velocity selector discussed in Section 3.5.2 and the acceleration column discussed in Section 4.2. The accelerator column ring size has been changed from 15 cm to 8 cm to get a more representative simulation, the rest of the dimensions were kept the same for all components. A schematic view of the geometry of the accelerator components is shown in Figure 3.7.

The simulations were run for U_t=1.5 and 2.5 MV, and U_e=10, 12.5 and 15 kV. The ion source output beam described in Section 3.3.3 was used with a KV sampling distribution and 1e4 particles. A parametric sweep was used to iterate over the combinations of U_e and U_t. In addition to the envelope and phase spaces, the fraction of particles that make it through the aperture, called the APR (Aperture Pass Ratio) is calculated. The APR is expressed as:

$$APR = \frac{n}{N}, \tag{3.15}$$

where APR is ratio of the number of particles that reach the end of the accelerator (n), to the number of input particles (N).

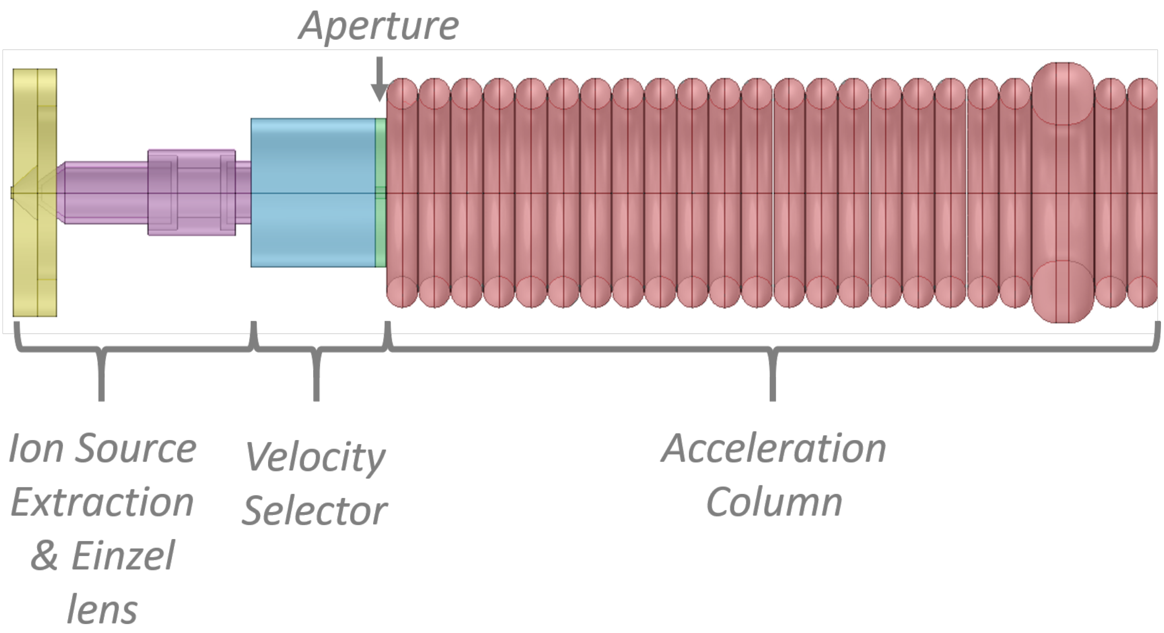

Figure 3.7: Schematic of the geometry used in COMSOL for the full simulation. Only one section of the acceleration column is shown.

4 Results

This chapter outlines the major results of this work and is divided into three sections, each section addressing one of the three key project goals that are stated in Section 1.1. Section 4.1 discusses the results generated from the comparison of simulation codes, for which methodology is discussed in Section 3.4. The results of the independent component modelling, for the LIBAF Pelletron, can be found in Section 4.2, with the approach discussed in Section 3.5. Section 4.3 presents results from the incorporation of the independent components into a full source-to-exit simulation of the LIBAF Pelletron, the methodology for which is detailed in Section 3.6.

4.1 Comparison of Simulation Codes

4.1.1 Input Beam

The initialisation of the Gaussian sampled phase space, using the Test-Beam described in Section 3.3.2, was compared for the three software packages. Results are shown in the phase plot in Figure 4.1 and the corresponding ellipse dimensions with statistical uncertainty are shown in Table 4.1.

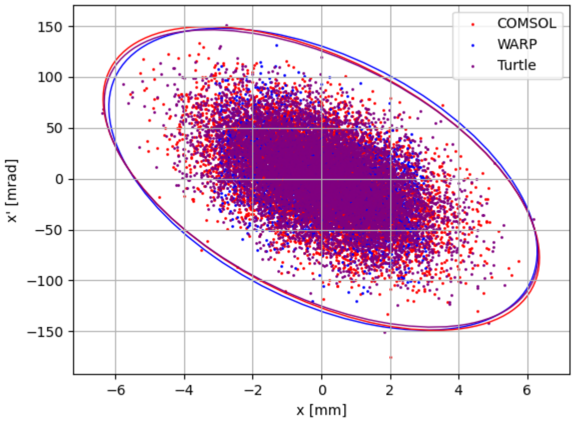

Figure 4.1: Comparison of the Gaussian input Test-Beam for the different software packages. Particle distributions are indicated by the coloured dots for each software package. The ellipses of corresponding colour, are fitted to the particle distributions at $4\sigma_s$.

The maximum variation between any two packages is less than 1% for variables R_1 and θ. Between WARP and TURTLE, R_2 and ϵ vary by less than 1%, but COMSOL shows a variation of ∼3% for each of these variables. In the case of ϵ, this 3% difference is within the $1\sigma_s$ of the uncertainty. For R_2 the 3% difference falls within $2\sigma_s$.

Table 4.1: Measured phase space parameters for a Gaussian input beam at 1σ for the three software packages. Only statistical uncertainties are reported.

Parameter	**COMSOL**	**WARP**	**TURTLE**
$R_1[\sqrt{mm^2+1}]$	0.250 ± 0.002	0.249 ± 0.002	0.251 ± 0.002
$R_2[\sqrt{mm^2+1}]$	106.6 ± 0.8	103.5 ± 0.7	103.2 ± 0.2
$\theta[rad]$	0.022 ± <0.001	0.019 ± <0.001	0.022 ± <0.001
$\epsilon[mm]$	84.0 ± 0.8	81.0 ± 0.8	81.0 ± 0.8

4.1.2 Lattice Simulations

The resulting envelopes and phase spaces from the Lattice simulations described in Section 3.4.3 are presented in Figure 4.2, and Figure 4.3 respectively. The envelope shown for WARP in Figure 4.2 is that generated by the envelope solver.

For the first drift element extending to z=0.5 m, the three software packages are indistinguishable. The hard-edged nature of the lattice simulations can clearly be seen by the separation of the drift and acceleration with the turn over point at z=0.5 m. In the second region where the acceleration is defined, TRANSPORT shows a very strong focusing effect compared to both WARP and COMSOL. At the end of the column (z=1 m) a difference of $\approx$ 20% can be observed for COMSOL and WARP which also can be observed in the phase plot seen in Figure 4.3.

In Table 4.2 the ellipse parameters are shown at z=1 m. The variation between WARP and COMSOL in R_1 is 13.2% and for R_2 it is ~82%. The resulting ϵ from warp is more than six times higher compared to COMSOL.

4.1.3 Simulations Based on 3D Geometry

Figure 4.4 shows the electric field and the potential for the 3D simulation as discussed in Section 3.4.4. A clear difference is observed compared to the lattice simulation, the potential lines in the 3D simulation extend into what was formerly a drift region in the lattice simulation. This causes the field to be continuous over the whole simulation region. The beam envelope of the 3D simulation can be seen in Figure 4.5, for TURTLE, WARP and COMSOL. For COMSOL and WARP it is clearly shown that the hard-edge effects of the fields have disappeared and the focusing effect due to the acceleration is smoothed out.

In Figure 4.6(a) and Figure 4.6(b), the z=0 m and z=1 m phase plots are shown respectively. The corresponding ellipse parameters are described in Table 4.3. As can be seen from these data, ellipse parameters vary significantly between the packages. Notably, the angle of the phase ellipse in TURTLE disagreeing with COMSOL and WARP. Variations in ϵ predicted can be seen to be larger at z=0.5 m than at z=1.0 m.

4.1.4 Energy Convergence Study

The envelope results for a selection of energies of the beam energy convergence study, discussed in Section 3.4.5, can be seen in Figure 4.7. At 30 keV a strong focusing effect is shown in TURTLE, the focal point is positioned in the simulation region at ~0.87 m. The same effect, although less apparent, is observed for COMSOL and WARP where the focal points are located outside the simulation region. For higher energies the divergence increases in all

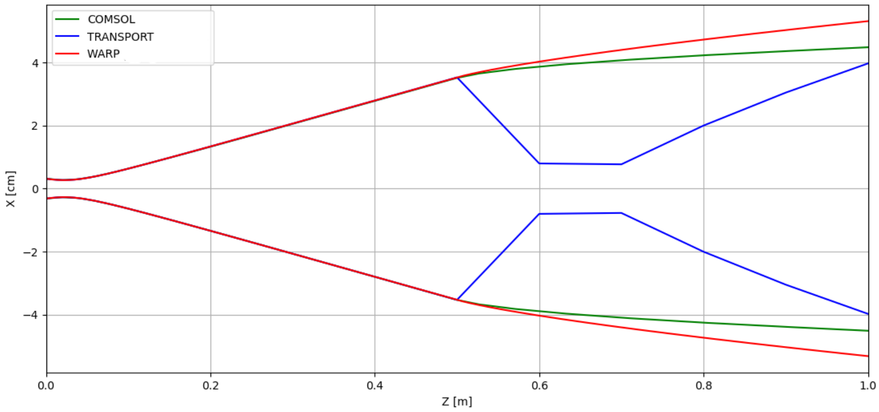

Figure 4.2: Beam envelopes in a 0.5 m field free region followed by a 0.5 m acceleration region, with an applied potential of 1.25 MV.

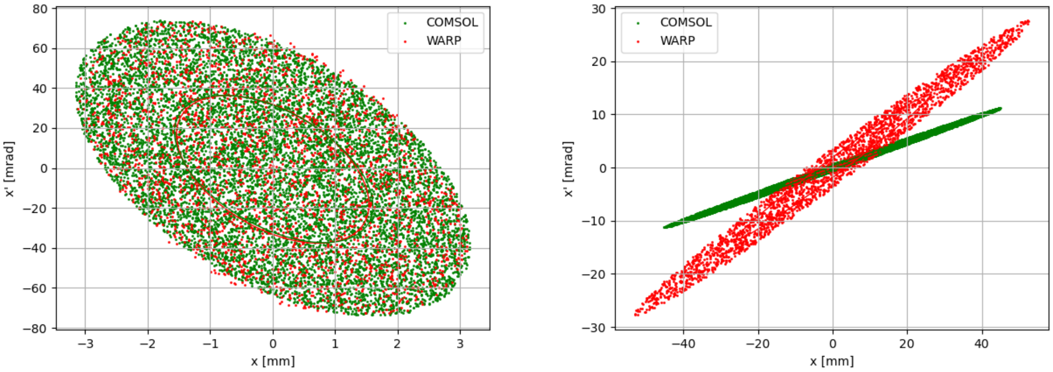

(a) **(b)**

Figure 4.3: Phase spaces of the KV sampled test beam used for the lattice simulation of the 0.5 m drift, 0.5 m acceleration test, in both COMSOL and WARP. Coloured dots indicate the sampled particles. (a) The phase spaces at the start of the simulation (z=0 m). (b) Phase spaces at the end of the simulation (z=1 m).

Table 4.2: Results for the ellipse parameters with uncertainties for the WARP and COMSOL phase spaces.

Parameter	**COMSOL**	**WARP**
$R_1[\sqrt{mm^2+1}]$	31.87 ± 0.22	36.72 ± 0.26
$R_2[\sqrt{mm^2+1}]$	0.24 ± <0.01	1.35 ± <0.01
$\theta[rad]$	1.82 ± 0.013	2.05 ± 0.014
$\epsilon[mm]$	24.25 ± 0.24	156.18 ± 1.55

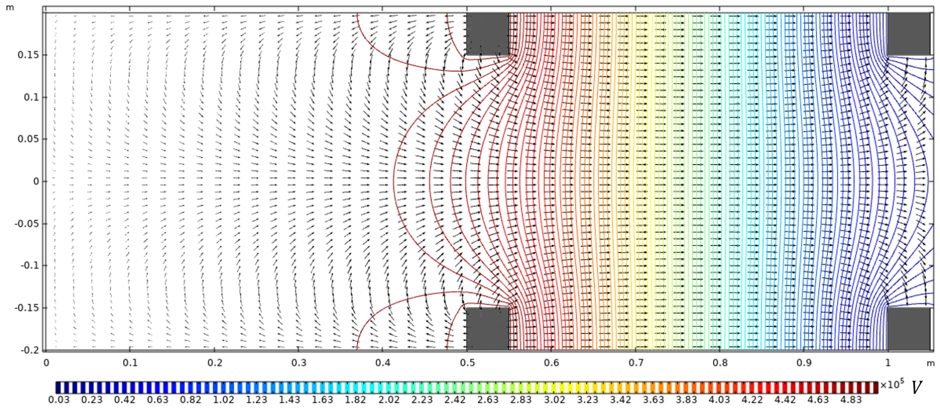

Figure 4.4: A 2D (z, y) cut-plane in COMSOL, showing the electric field lines as logarithmically sized arrows and the contours of the potential, in the 3D test geometry simulation. The two rings to which potentials are applied are indicated in dark grey.

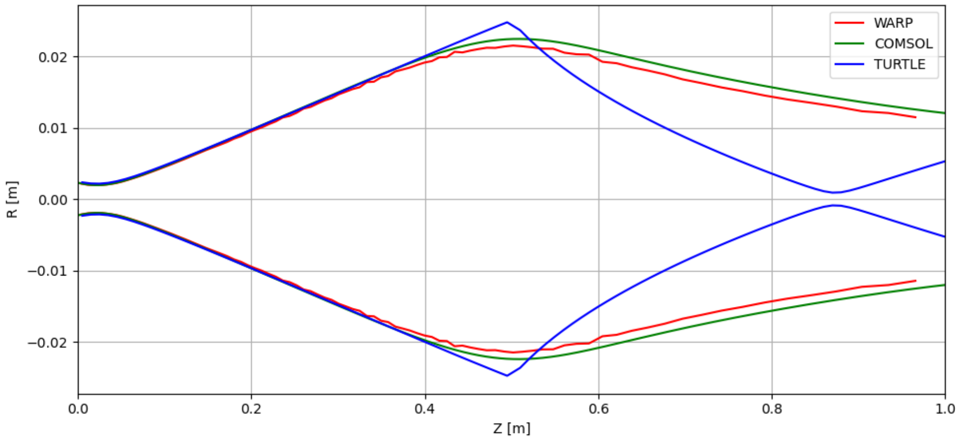

Figure 4.5: The beam envelopes at $r = 1\sigma_s$ for WARP, COMSOL and TURTLE, simulated for the 3D test geometry.

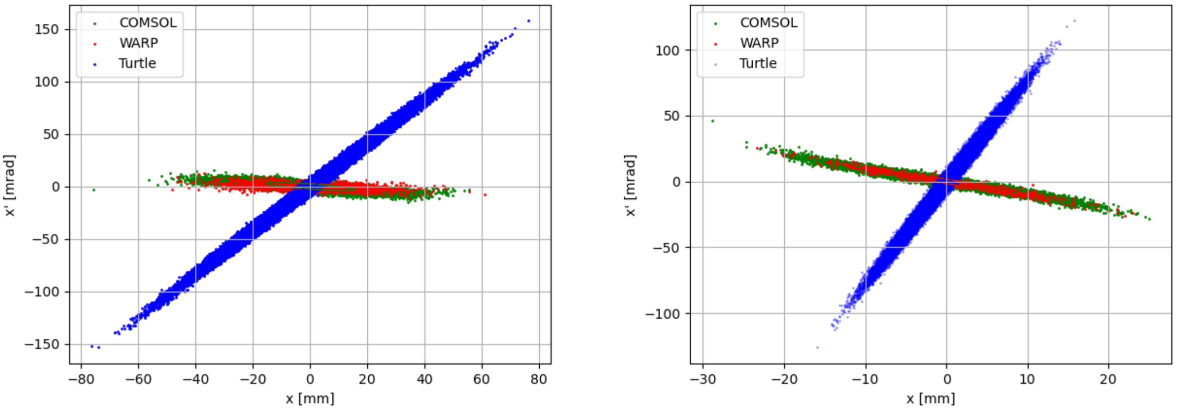

(a) Phase space at z =0.5 m

(b) Phase space at z =1.0 m

Figure 4.6: Phase spaces at two locations in the 3D test geometry simulation for WARP, COMSOL and TURTLE. Ellipses are indicated by the same colour, the parameters of which are presented in Table 4.3.

Table 4.3: Fitted ellipse parameters of the phase spaces predicted by each package, at two values of z, for the 3D test geometry. Uncertainties given are statistical. The phase spaces are depicted graphically in Figure 4.6.

z (m)	Parameter	COMSOL	WARP	TURTLE
0.5	$R_1[\sqrt{mm^2+1}]$	7.30 ± 0.05	11.07 ± 0.08	24.98 ± 0.20
	$R_2[\sqrt{mm^2+1}]$	5.22 ± 0.04	3.65 ± 0.03	2.01 ± 0.01
	$\theta[rad]$	1.37 ± 0.01	1.48 ± 0.01	-0.45 ± 0.01
	$\epsilon[mm]$	119.79 ± 1.19	127.25 ± 1.26	157.58 ± 1.56
1.0	$R_1[\sqrt{mm^2+1}]$	1.23 ± <0.01	1.17 ± <0.01	5.06 ± <0.01
	$R_2[\sqrt{mm^2+1}]$	10.43 ± 0.07	11.11 ± 0.08	2.34 ± <0.02
	$\theta[rad]$	0.79 ± <0.01	0.77 ± <0.01	-0.13 ± <0.01
	$\epsilon[mm]$	40.37 ± 0.40	40.69 ± 0.40	37.13 ± 0.37

software, where the focal point for energies $<$ 30 keV is positive and $>$ 300 keV is negative.

To extract the focal lengths and divergences for the full range of energies as discussed in 3.4.5, a linear function is fitted to the resulting envelope data in the region 0.7 <z< 0.8 m. In Figure 4.8(a) the gradients of the linear fits are plotted as a function of the initial beam energy. Most notably it shows that the crossover point, where the divergence is zero and hence, $f = \infty$, is located at ∼100 keV. Figure 4.8(b) shows the focal point or y=0 intersect as a function of energy. The function $f = a/(bU_e + c)$ was fitted to the data to obtain the $f = \infty$ point, visible at ∼100 keV for both COMSOL and WARP.

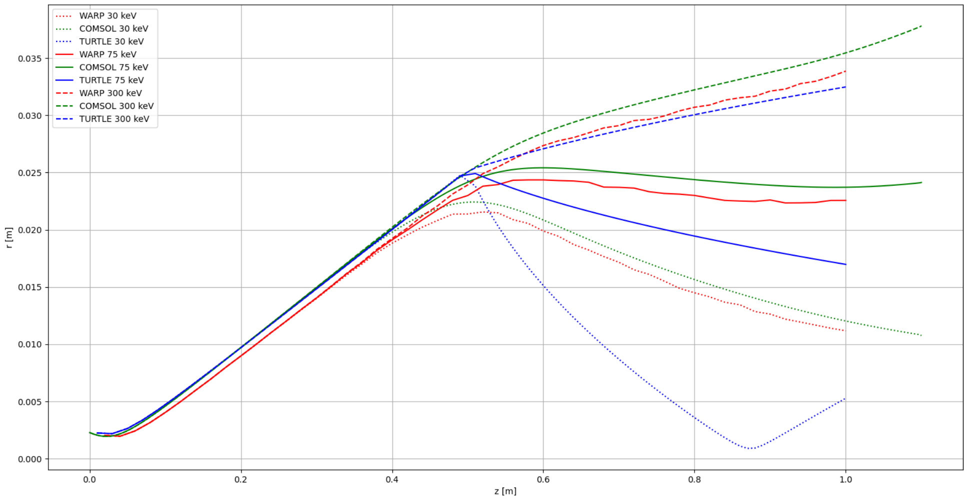

Figure 4.7: Beam envelopes for the beam energy study, a subset of U_{in} = [30 keV, 75 keV, 300 keV] is plotted. Different line styles indicate the three software packages, COMSOL, WARP and TURTLE.

4.1.5 Space Charge

A study on the space charge effects was performed in COMSOL according to Section 3.4.6. The self potential of the beam was modelled for a selection of currents, Figure 4.9 showing

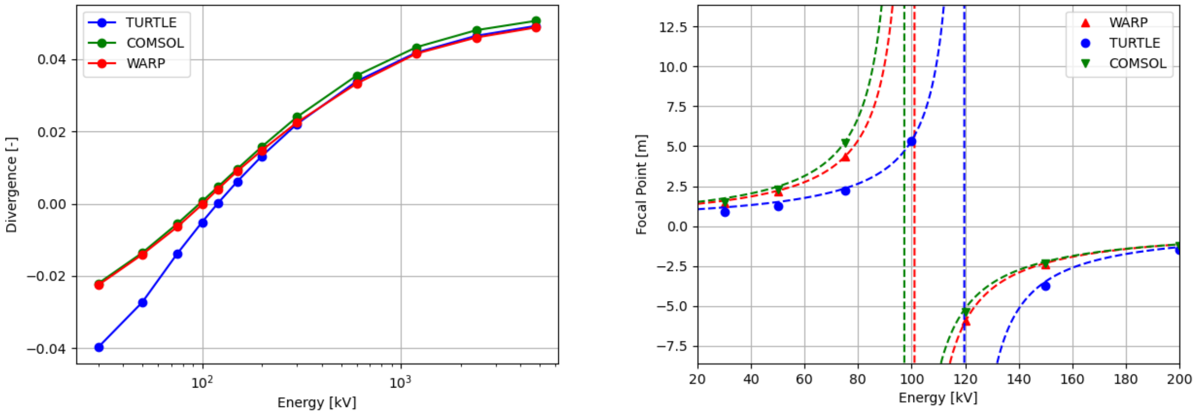

(a) Energy gradient. **(b)** Focal point.

Figure 4.8: The divergence and focal point for the beam energy study for different initial energies, for each of the three software packages. In figure (a) the solid lines are plotted to guide the eye while in (b) the dotted lines indicate a function $f = a/(xU_e + c)$ with coefficients fitted for each data set.

the resulting self potential of the beam as function of z. The beam envelopes, resulting from the initial divergence and the divergence caused by the space charge effects are shown in Figure 4.10(a) for a variety of currents. In Figure 4.10(b) the variation relative to the non-space charge (NSC) simulation is shown. At a current of ∼1 mA, corresponding to a general perveance of $1.25e-4$, a deviation in x of ∼4% is observed.

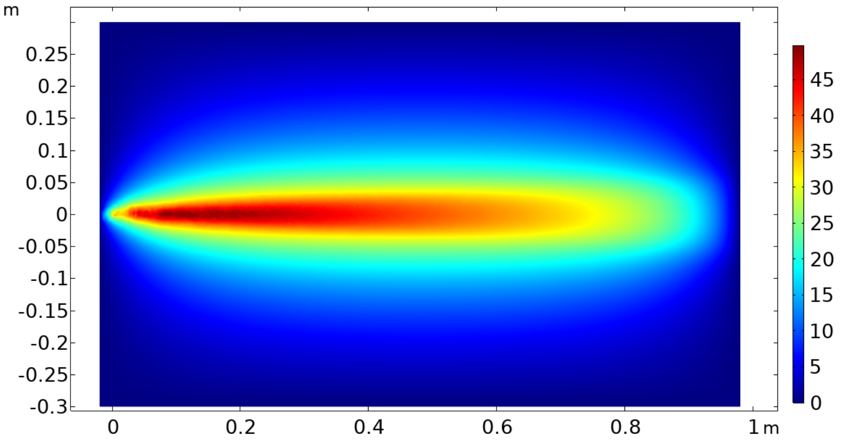

Figure 4.9: Self potential of the beam, in the space charge study, caused by the coulombic repulsion of the ions within the simulation region. The potential goes down as the beam diverges at higher values of z. The color-mapping indicates the potential in V.

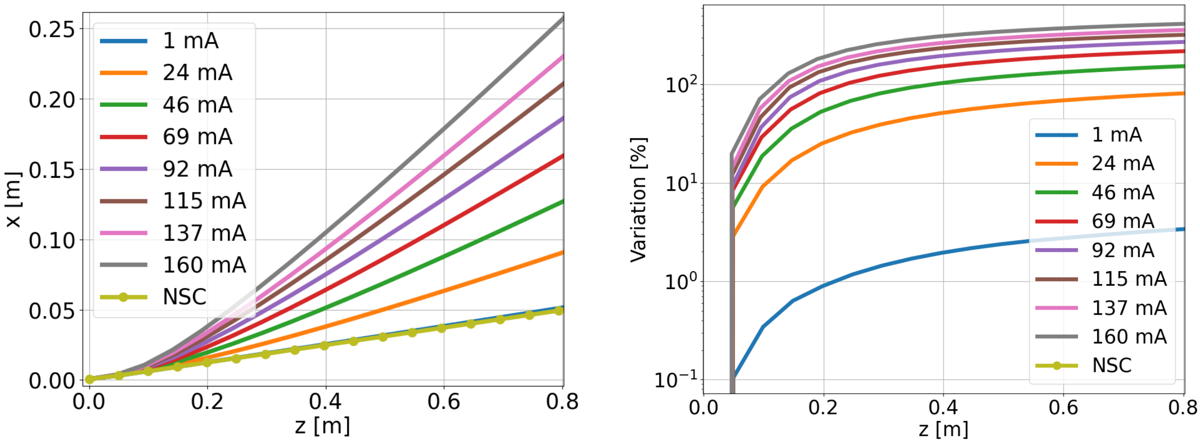

(a)

(b)

Figure 4.10: (a) Effects of space-charge in a 1m drift simulation in COMSOL. (b) The variation compared to the non-space charge envelope (NSC) as a function of z for different currents.

4.2 Acceleration Components

4.2.1 Acceleration Column & Mesh Convergence

Mesh Convergence

A mesh convergence study was performed in WARP and COMSOL, details of which are provided in Section 3.5.1. The mesh quality reported, is a range from 1 to 4, which corresponds to the mesh sizes used in the software: Normal, Fine, Finer and extra fine and cell numbers of |50|50|75, 100|100|150, 200|200|300 and 400|400|600, for COMSOL and WARP respectively.

The effect of the mesh quality on the construction of the geometry in WARP can be seen in Figure 4.11. In Figure 4.11(a), the 50|50|75 cell distribution results in the geometry being barely visible. In Figure 4.11(b), the 400|400|400 mesh clearly resolves the geometry of the rings. The equipotential lines are distributed more evenly in the region at the higher cell division. In Figure 4.12(a) and 4.12(b), the geometry created in COMSOL can be seen for a normal- and extra fine-mesh respectively. The geometry shown in Figure 4.12(b), consists of smaller element sizes and is therefore represented in a more continuous way.

The beam envelopes, resulting from the particle tracing through the acceleration column can be seen in Figure 4.13(a) for COMSOL and in Figure 4.13(b) for WARP. The variation in the envelope for the different mesh granularities of COMSOL was less than 1% at the end of the acceleration column. In WARP the variation between the lowest and highest mesh quality is ∼10%.

As can be seen in Figure 4.14(a), values of R_1 for COMSOL remain constant within statistical uncertainty, while for WARP a decrease of 10% is observed between the lowest and highest mesh quality. For R_2, which can be seen in Figure 4.14(b), COMSOL shows a variation of about 30% and WARP shows no significant variation at different mesh qualities. For θ, shown in Figure 4.14(c), values are constant within statistical uncertainty for both WARP

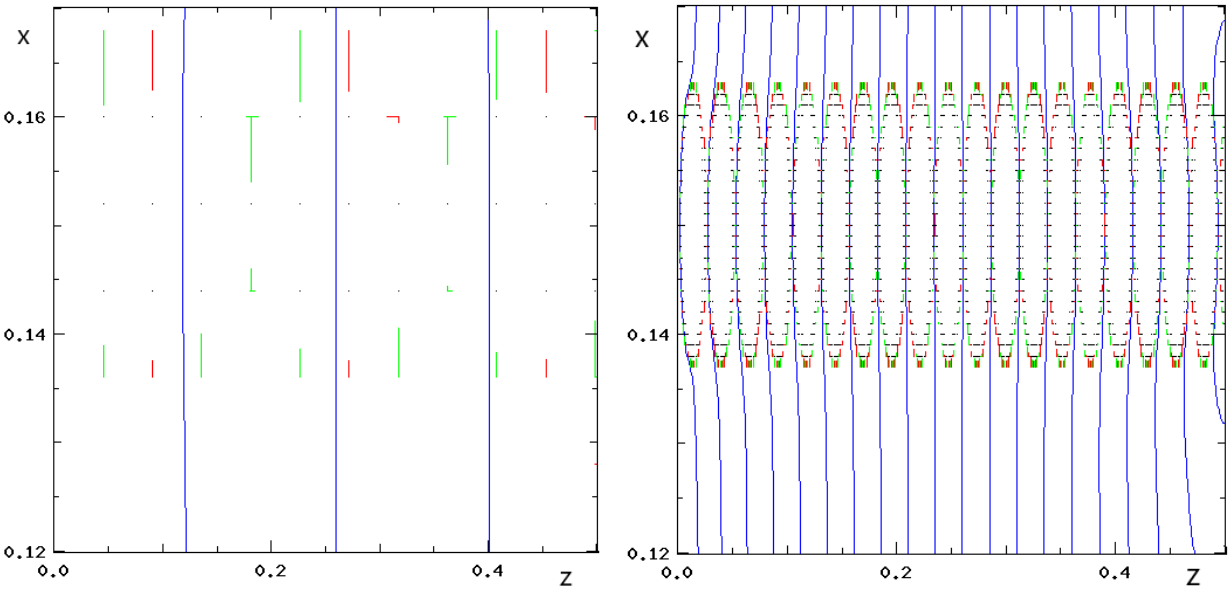

(a) Cell distribution of 50|50|75 **(b)** Cell distribution of 400|400|400

Figure 4.11: Impact of the cell distribution on the acceleration column geometry in WARP for two different cell distributions, shown in a (z, x) 2D cutplane. The red and green lines indicate the boundaries of the geometry. The blue curves show the equipotential lines.

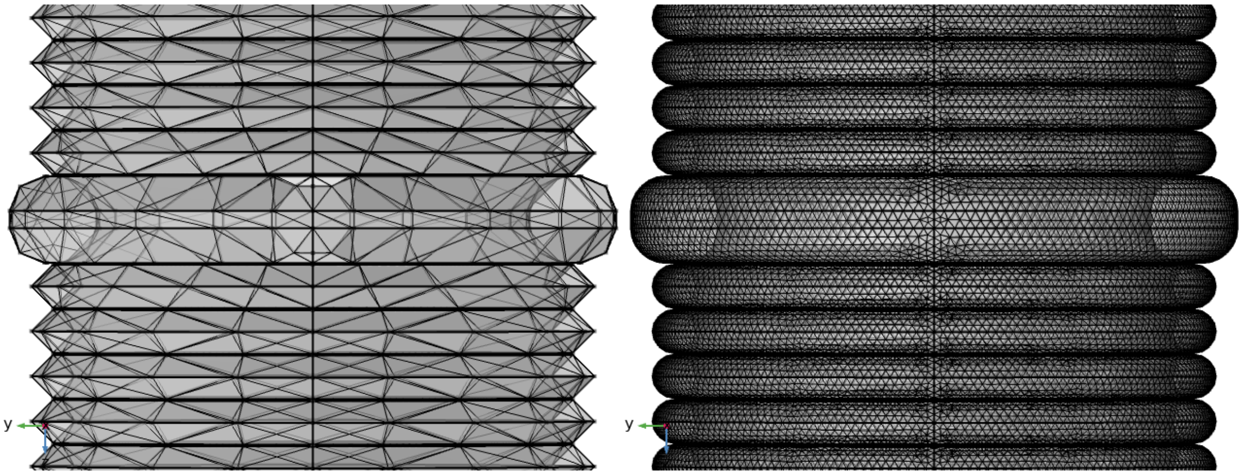

(a) Normal mesh geometry **(b)** Extra fine mesh geometry

Figure 4.12: Impact of the mesh size on the geometry in COMSOL for two different mesh granularities, for a subsection of the acceleration column.

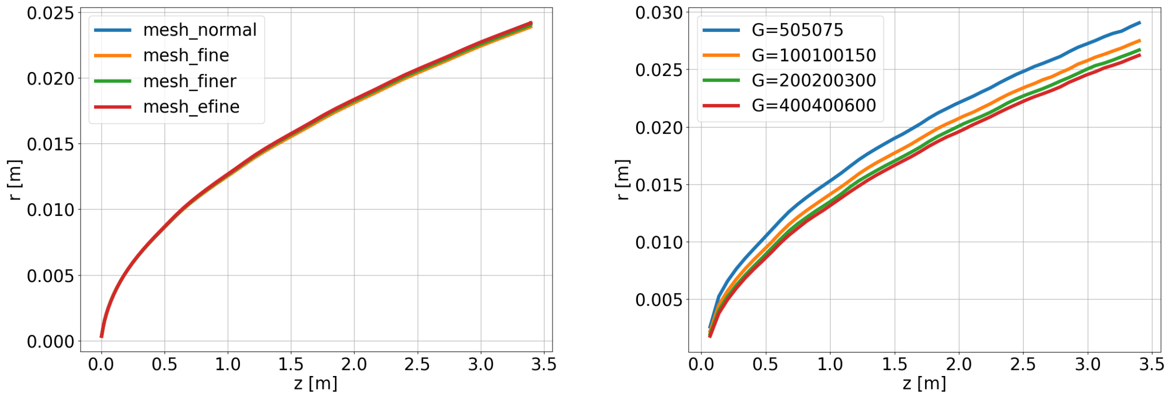

(a) COMSOL **(b)** WARP

Figure 4.13: Effect of the mesh quality size on the beam envelopes, predicted by (a) COMSOL and (b) WARP, in the mesh convergence study.

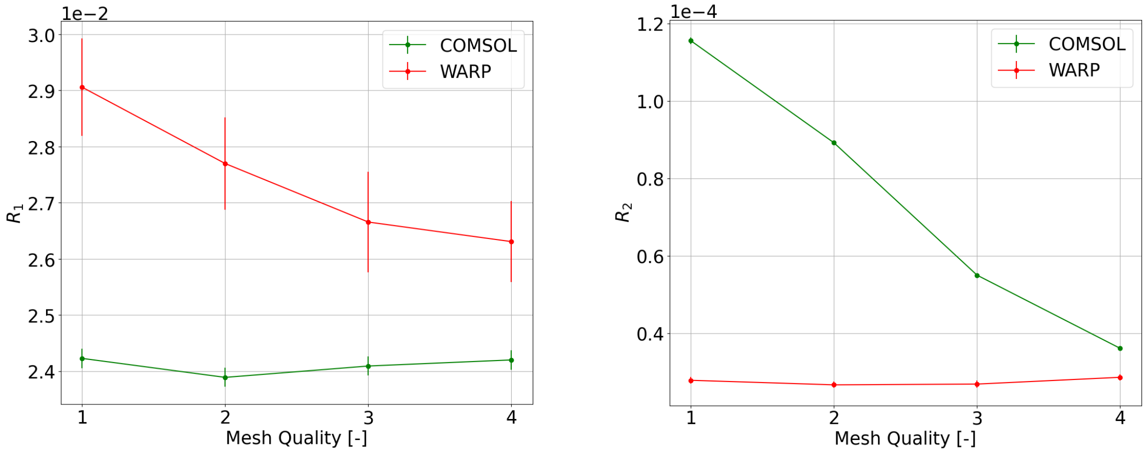

(a) R_1 **(b)** R_2

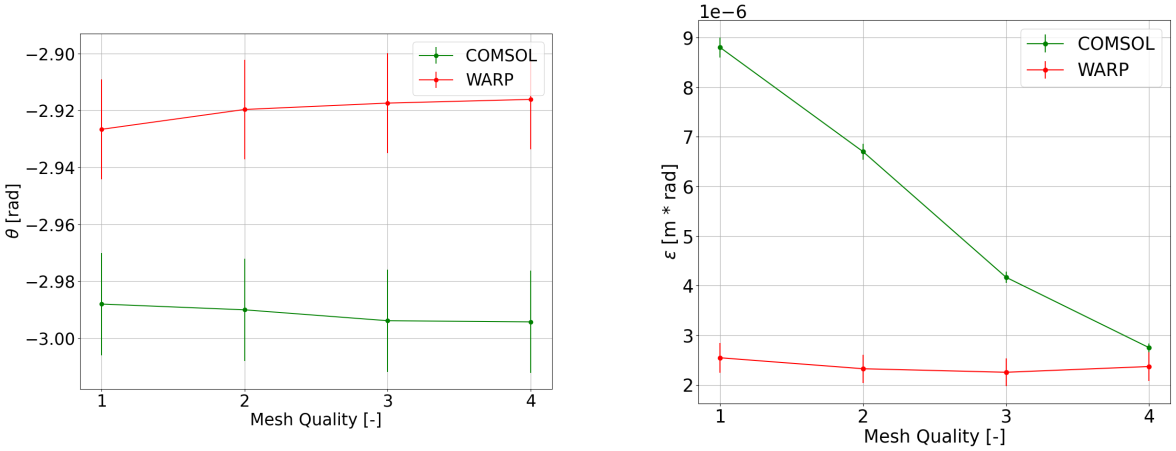

(c) θ **(d)** ϵ

Figure 4.14: Fitted ellipse parameters of the phase spaces predicted by COMSOL and WARP, at several mesh quality. Vertical lines indicate statistical uncertainties. Lines between points are to guide the eye.

and COMSOL. The resulting ϵ can be seen in Figure 4.14(d), with values from COMSOL clearly converging towards those from WARP with a decrease of 30%, about 10% per mesh quality step. For WARP, values of ϵ are constant within statistical uncertainty.

The simulation times for the three software packages at the different mesh qualities are summarized in Table 4.4. As the mesh quality increases, the simulation time is increased. For COMSOL the simulation time increases by a factor of 3.5 if the mesh quality is increased from normal to extra fine. For WARP the simulation time increases by a factor of around 1.5 when the cell division is increased from 50|50|75 to 400|400|400. Notably the simulation time for TURTLE is much lower than both COMSOL and WARP.

Table 4.4: Simulation times of the packages at different mesh granularities for COMSOL and different cell divisions in WARP. The mesh quality definitions are given in Section 4.2.1. The simulation time reported for TURTLE uses a total ray count of 10e6.

Mesh Quality	COMSOL	WARP	TURTLE
1	183 s	4620 s	27.12 s
2	189 s	5666 s	
3	191 s	6200 s	
4	633 s	7186 s	

Acceleration Column

In Figure 4.15 the envelope of the Gaussian beam, propagating through the geometry of the acceleration column, is presented. The divergence as a result of the acceleration in COMSOL is slightly less then modelled by TURTLE, however, within a 2.5% margin. The divergence in WARP is modelled to be larger than both TURTLE and COMSOL by ~6%.

The phase spaces for the three different software packages at the end of the acceleration column ($z \approx 3.4$) are presented in Figure 4.16. The corresponding parameters describing the fitted ellipses are presented in Table 4.5. For COMSOL R_1 varies by ~2.4% to TURTLE while it varies by ~32% to WARP. While the for COMSOL R_2 varies around 20% to WARP and 30% to TURTLE, WARP and TURTLE differ by only 10%. θ appears to be very similar for WARP and TURTLE, with difference of only 0.2%, for COMSOL is it ~3%.

4.2.2 Velocity Selector

Results from the proof of principle simulation of the velocity selector, discussed in Section 2.2.3, can be seen in figures 4.17 and 4.18. For the monochromatic pencil and input beams, seen in Figure 4.17, it can be seen that the electric and magnetic forces are the same for E_0 =50 keV with a filter energy of 50 keV, not affecting the envelope at all. When E_f is set to 100 keV the pencil and input beams are displaced by ~7.5 mm in the $+x$ direction by the electric field. In Figure 4.18 the phase space for the velocity selector is shown. The filtering effects are apparent for both the pencil beam and the input beam with an input energy of 50 keV. As E_f is changed from 50 keV to 100 keV a diagonal shift of 1 cm in the phase space is observed.

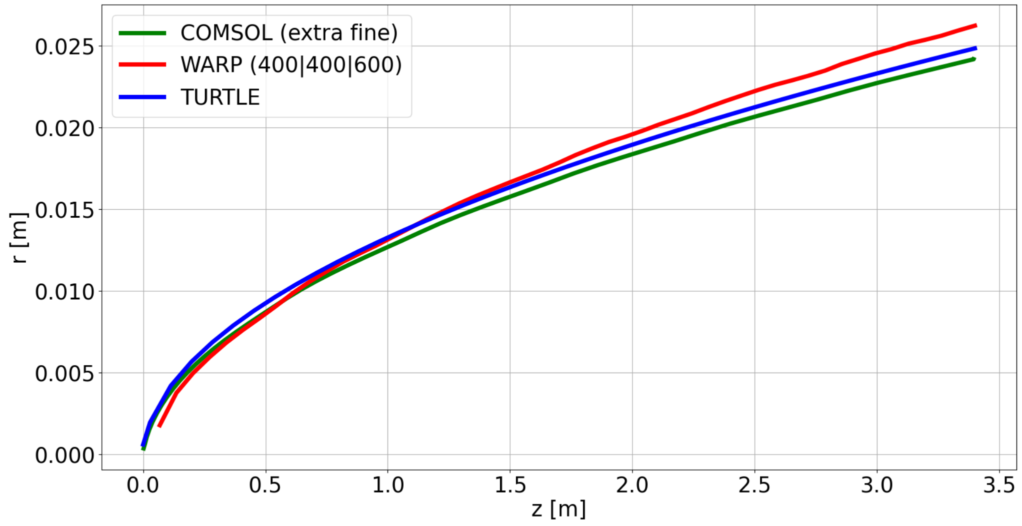

Figure 4.15: The $1\sigma_s$ beam envelope through the acceleration column for the highest mesh granularity/cell division for COMSOL and WARP, as well as the beam envelope predicted by TURTLE.

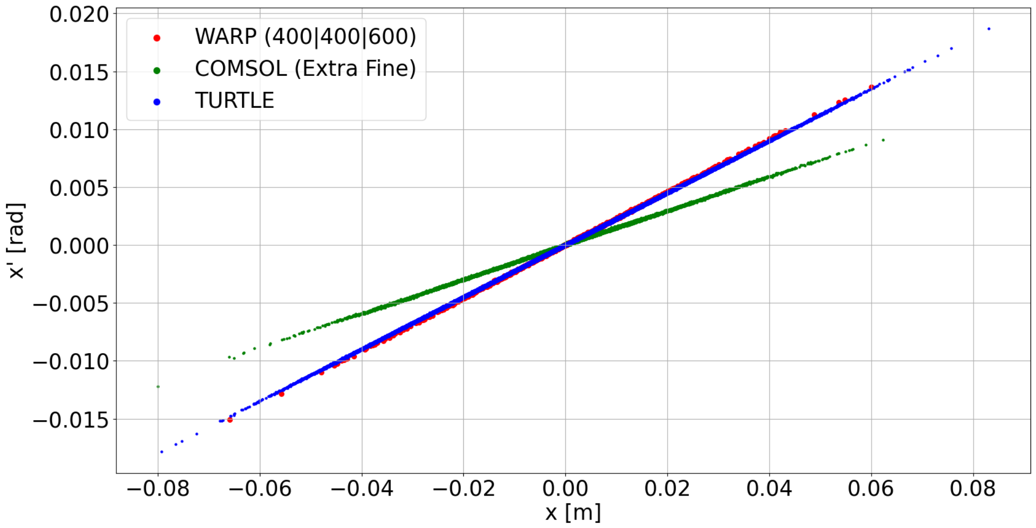

Figure 4.16: Phase space predictions for the end of the acceleration column, produced in TURTLE and for the highest mesh granularity/cell division for COMSOL and WARP.

Table 4.5: Fitted ellipse parameters for the phase space at the end of the acceleration column ($z \approx 3.4$ m).

Parameter	**COMSOL**	**WARP**	**TURTLE**
$R_1[\sqrt{mm^2+1}]$	24.00 ± 0.17	36.00 ± 0.25	24.60 ± 0.17
$R_2[\sqrt{mm^2+1}]$	0.036 ± <0.001	0.029 ± <0.001	0.026 ± <0.001
$\theta[rad]$	3.00 ± 0.01	1.79 ± 0.01	1.79 ± 0.01
ϵ [μm]	2.75 ± 0.03	2.37 ± 0.02	2.00 ± 0.02

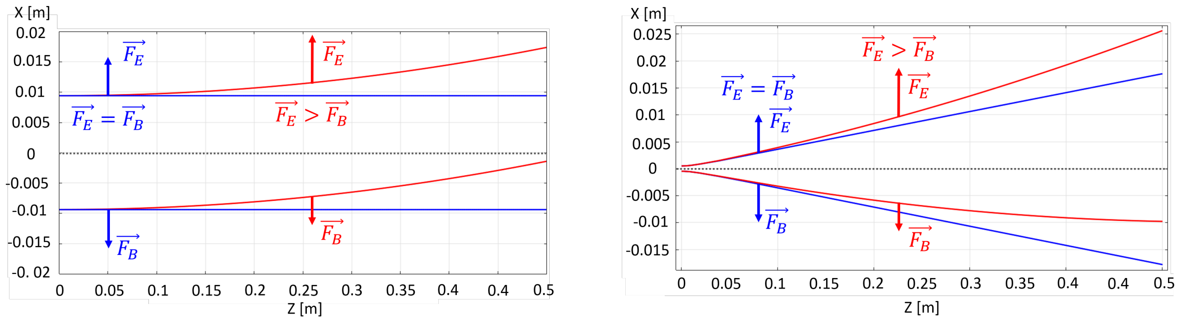

(a) Pencil beam.

(b) Input beam.

Figure 4.17: Envelopes of the proof of principle simulation for the velocity selector. Blue and red lines indicate the envelopes for $E_f = E_0$ and $E_f = 2E_0$ respectively. Forces, expressed by the coloured arrows, are shown for the corresponding filter energies.

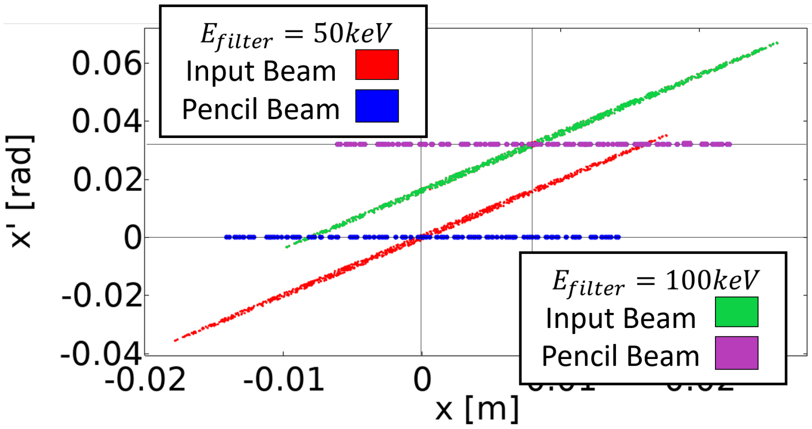

Figure 4.18: Phase space plots for the proof of principle simulation of the velocity selector, for a pencil- and input-beam at two different filter energies.

4.2.3 Ion Source Extraction & Einzel Lens

The beam envelope results of the ion source extraction and Einzel lens simulation, described in Section 3.5.3, can be seen in Figure 4.19. $f \approx 5$ cm is seen for U_e=20 kV, with a varation of 13% is observed between COMSOL and WARP. For U_e=15 kV a focusing is observed for both WARP and COMSOL, with $f > 0.3$ m. At U_e=10 kV f is negative, for both WARP and COMSOL. For the 10 kV and 15 kV envelope a variation of 3% is seen between WARP and COMSOL.

Phase space plots at the end of the Einzel lens ($z \approx 0.3$ m), for U_e=10, 12.5 and 15 kV, can be seen in Figure 4.20 and the phase ellipse parameters in Figure 4.21. For U_e=10 kV, a 2% difference is seen for R_1. At 12.5 kV, a difference of <1% is seen, and for 15 kV a difference of 7% is observed. For R_2 with U_e=10 kV, a difference of 14% is seen, 26% for R_2 at 12.5 kV and 2% at 15 kV, within $1\sigma_s$. For θ a variation of <1% is found for U_e=10 kV, within $1\sigma_s$, for 12.5 kV 5% and for 15 kV a variation less than 1% within $1\sigma_s$.

The focal points and divergences, resulting from the linear fits to the envelopes of the Einzel lens simulation, are shown in Figure 4.22. The Focal points are fitted with the function $f = a/(U_e b + c)$. The fitted function shows a crossover at a U_e of between 12.7 and 12.8 kV, a variation of 0.2% is found between COMSOL and WARP. For the divergences, a variation <1% is found for U_e<18 kV, a variation of 10% is observed for U_e =20 kV.

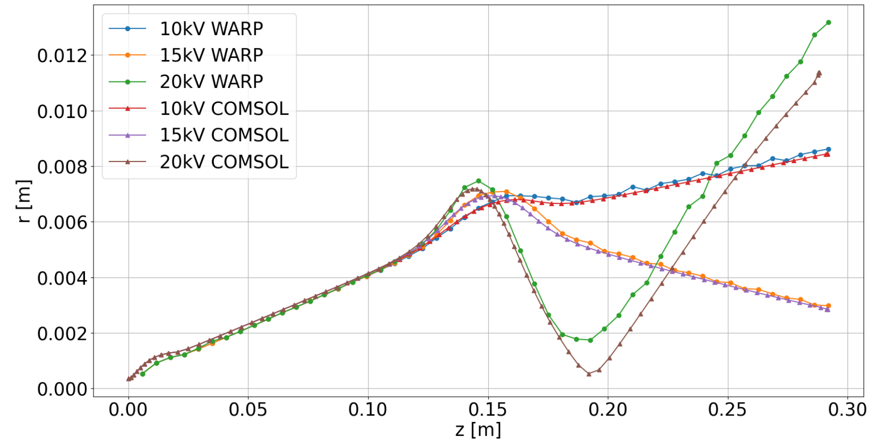

Figure 4.19: The $1\sigma_s$ beam envelope for the Einzel lens simulation, with selected values of U_e, for WARP and COMSOL.

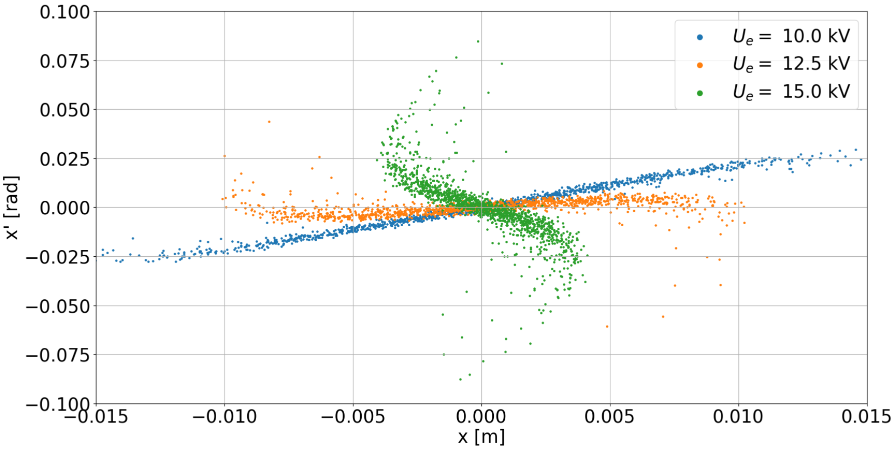

(a) WARP.

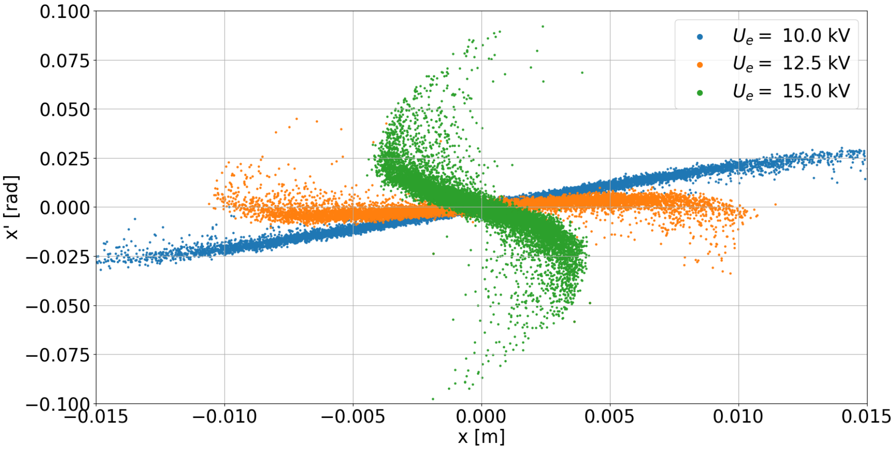

(b) COMSOL.

Figure 4.20: The phase spaces at the end of the Einzel lens simulation (∼0.3 m), in WARP and COMSOL. Colours indicate the different values of U_e used.

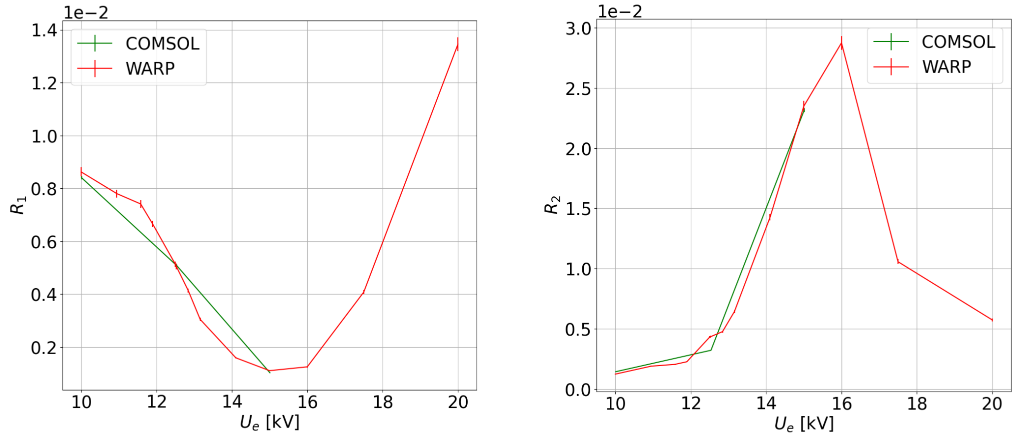

(a) R_1 **(b)** R_2

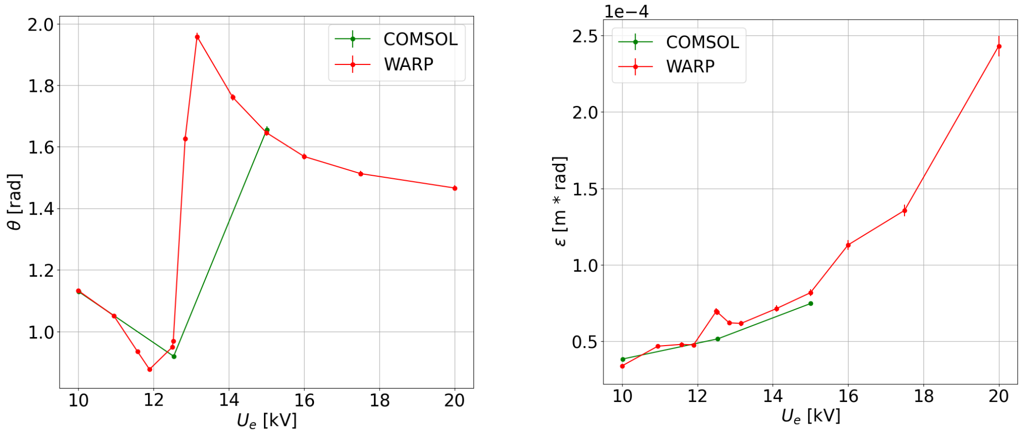

(c) θ **(d)** ϵ

Figure 4.21: Fitted ellipse parameters of the phase spaces predicted by COMSOL and WARP for the Einzel lens, with different values of U_e. Solid lines are shown to guide the eye. Statistical uncertainties are indicated by vertical lines, which in some cases are too small to be visible.

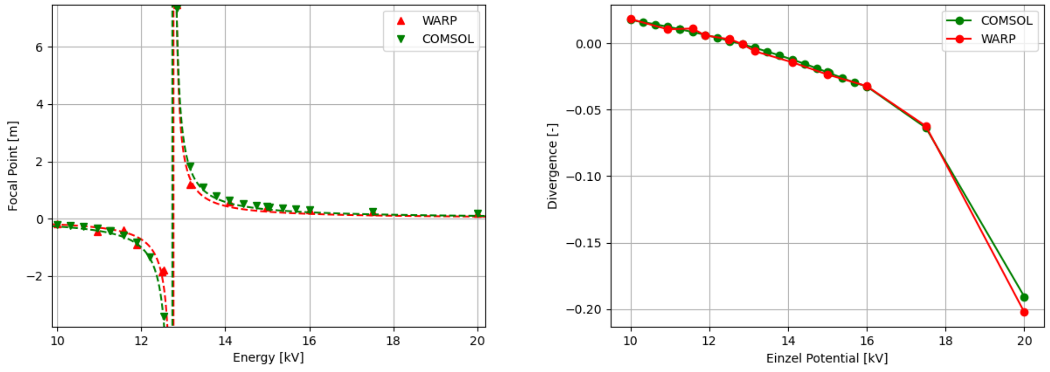

(a) Focal point. **(b)** Divergence

Figure 4.22: (a) Focal points of the Einzel lens as a function of U_e predicted by WARP and COMSOL, including fits to the data. (b) The divergence of the beams obtained by linear fits to the envelopes at different U_e for WARP and COMSOL.

4.3 Full Accelerator Simulation

4.3.1 Rendering

A simulation containing all LIBAF Pelletron components was created in COMSOL and run for different combinations of U_e and U_t as discussed in Section 3.6. The parametric sweep simulation took 9 hours, 30 min and 31 seconds to finish with the DESKTOP hardware described in Table 3.1.4. An example 3D rendering of the first 0.8 m of the geometry and propagation of the beam can be seen in Figure 4.23.

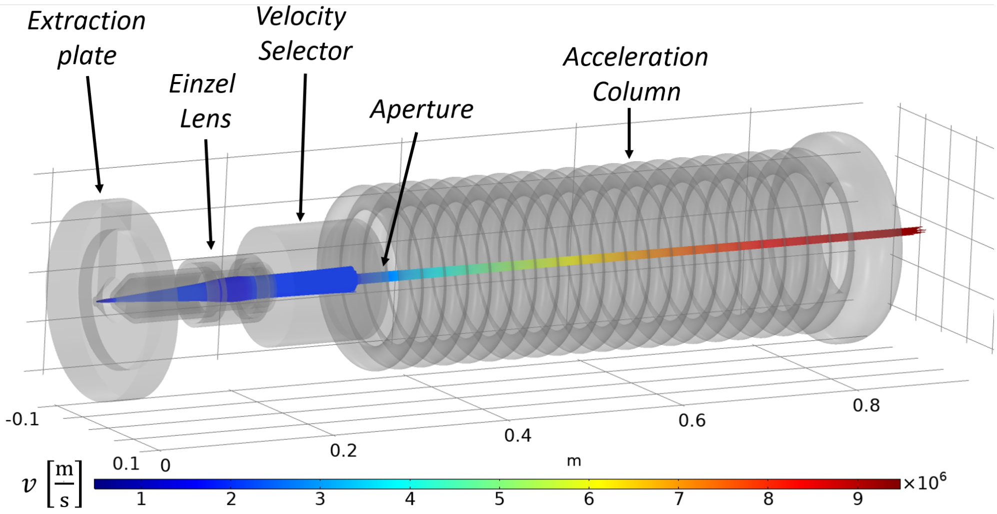

Figure 4.23: 3D rendering of the geometry and beam evolution through the simulation of the LIBAF Pelletron with U_e =15 kV and U_t =2.5 MV.

4.3.2 Beam Envelopes

In Figure 4.24 the beam envelopes can be seen for U_t=1.5 MV and U_e of 10, 12.5 and 15-kV. The envelope at 10 kV shows a profile enlargement of less than 3% while the envelope of the 12.5 kV shows a decrease in r of 51%. A divergent beam is created with U_e =15 kV, causing r to increase by seven times over the course of the acceleration column. At the start of the simulation, from z=0.0 to ∼0.25 m, the extraction can be seen followed by the Einzel lens, characterized by the focusing effect at around z=0.15 m. After focusing by the Einzel lens, the beam propagates through the velocity selector from z=0.17 to 0.27 m, eventually arriving at the aperture, where the beam is cut. The focusing of the Einzel lens has a large effect on the propagation of the beam after the aperture, as can be seen in Figure 4.24. A parallel beam is created at the end of the accelerator with values of U_e from 10 to 12.5 kV.

Similar results were obtained for the simulation with U_t=2.5 MV, which can be seen in Figure 4.25. A comparison of the U_t=1.5 and 2.5 MV envelopes shows a difference in r in the extraction region of less than 1%. At U_e =12.5 kV a difference in r of 7% is observed in the region immediately following the Einzel lens ($0.2<z<0.3$ m). At U_e =10 and 15 kV the variations are less than 2%. At the end of the column an increase of 100% in r is seen for U_e =10 kV. At U_e =12.5 kV the change of r is found to be less than 1%, and the increase in r for U_e =15kV is 18%.

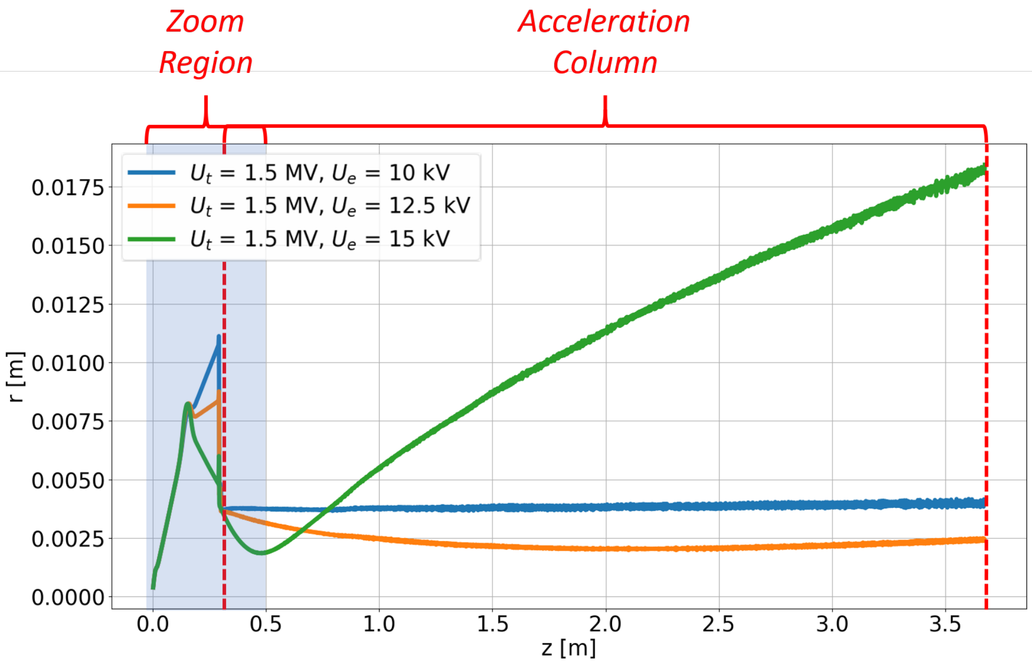

(a) Full envelope.

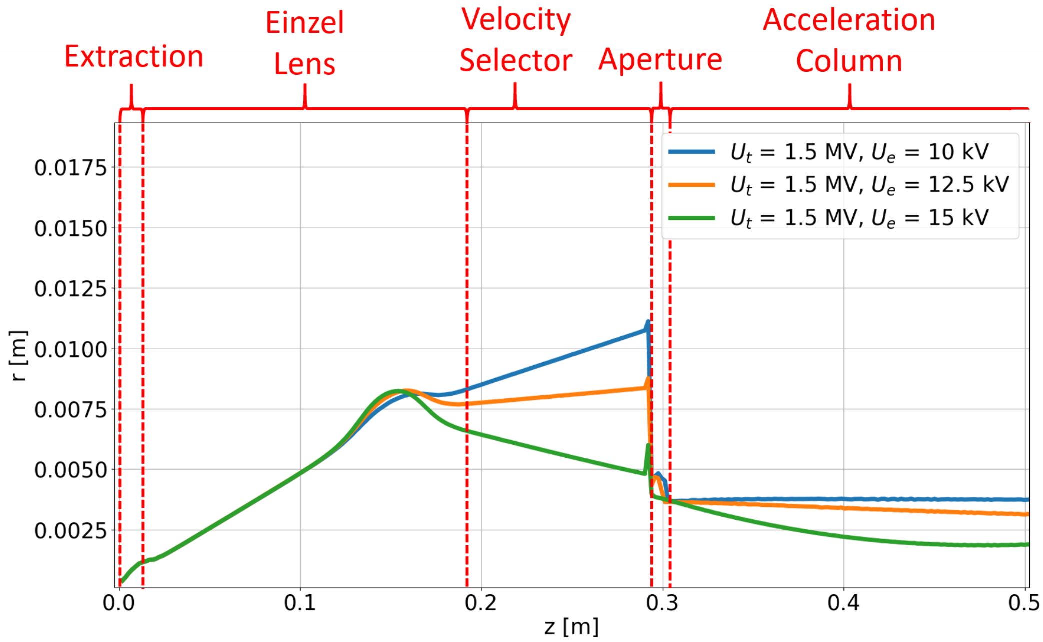

(b) Zoom region.

Figure 4.24: The KV beam envelope in r of the full simulation for U_t =1.5 MV. Colours indicate the different values of U_e. The zoom region indicated in (a) is shown in (b).

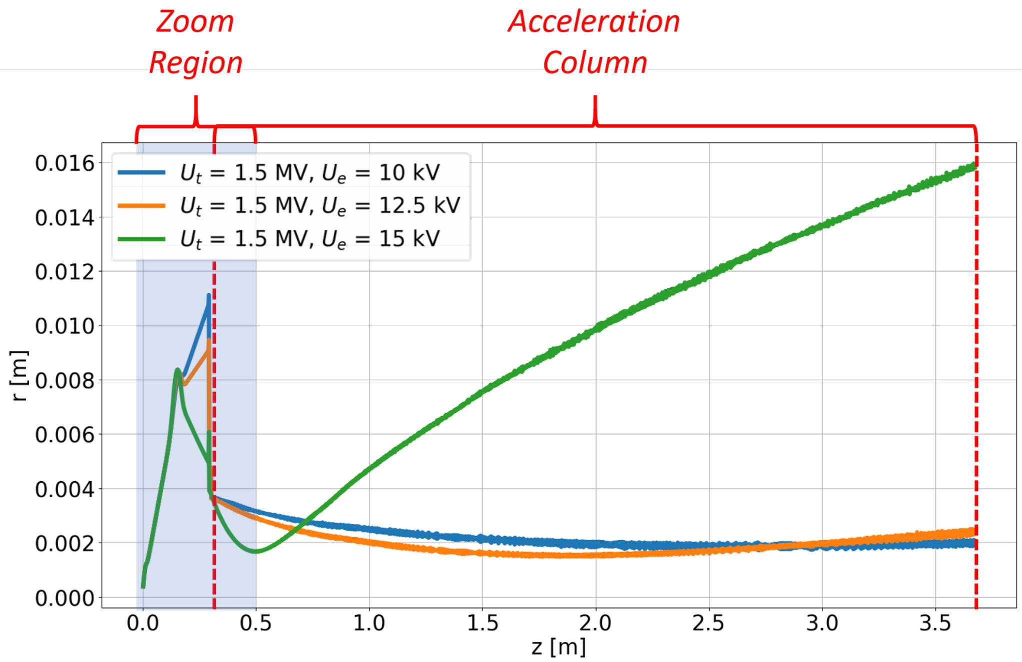

(a) Full envelope.

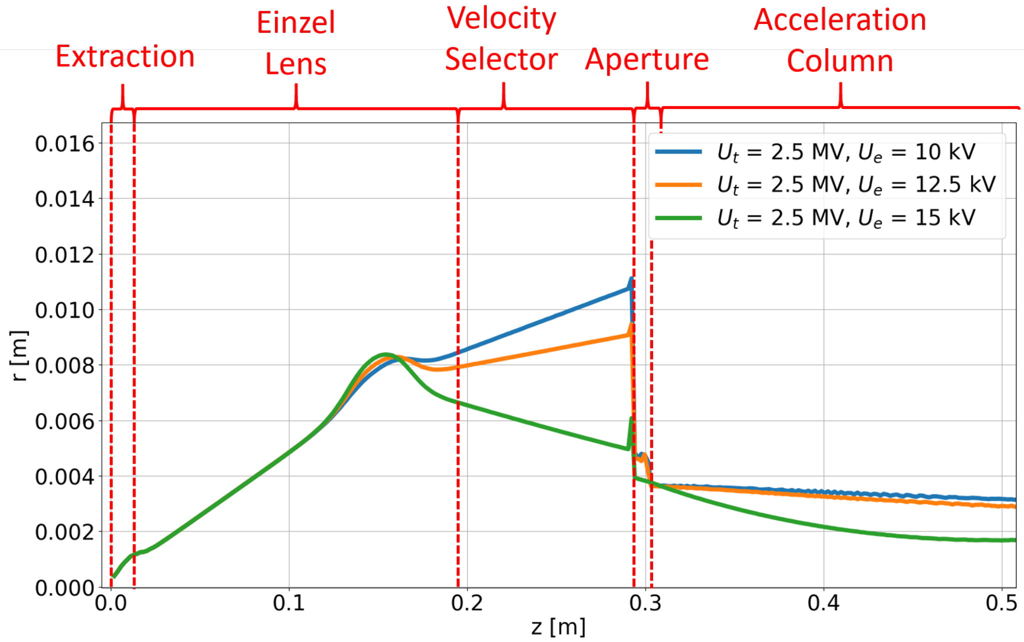

(b) Zoom region.

Figure 4.25: The KV beam envelope in r of the full simulation for U_t =2.5 MV. Colours indicate the different values of U_e. The zoom region indicated in (a) is shown in (b).

4.3.3 Phase Space

The phase space at the end of the extraction plate (z=0.02 m) can be seen in Figure 4.26. The phase space is the same for all values of U_e and U_t, as can be seen from the fitted ellipse parameters presented in tables 4.6 and 4.7.

The phase space at the end of the Einzel lens, for U_t=1.5 MV and U_t=2.5 MV, can be seen in Figure 4.27. Fitted ellipse parameters are shown in tables 4.6 and 4.7. For U_t = 10 kV the variation in R_1 between U_t = 1.5 and 2.5 MV is less than 5%, both within the $1\sigma_s$ uncertainty. At 12.5 kV the results vary by 8%. For R_2, the variation at U_e =10 and 15 kV is 4%, and 0.4% respectively. At 12.5 kV the contrast is 7%. The angle deviates 22% in the case of U_e =12.5 kV and 1% for 10 and 15 kV, both within statistical uncertainty. The resulting variation in ϵ in the case of 10 kV and 15 kV is 4%, and for 12.5 kV is less than 1%.

Figure 4.28 shows the phase spaces just after the aperture, at z=0.29 m, for U_t=1.5 and 2.5 MV. Fitted ellipse parameters are shown in tables 4.6 and 4.7. For U_t = 1.5 and 2.5 MV the difference observed for the R_1 value for the U_e, 47% for 10 kV, 30% for 12.5 kV and 6% for 15 kV. In R_2, the variation observed is 62% for 10 kV, 28% for 12.5 kV and less than 1% for 15 kV. For the angle a difference of $< 2\%$ is observed for 10 kV, 9% for 12.5 kV case and less than 1% for the 15 kV case, within statistical uncertainty. Values of ϵ show a variation of 27% at 10kV, 3% for U_e = 12.5 kV and 4 % for the 15 kV case.

Phase spaces at the end of the acceleration column (z=3.68 m), can be seen in Figure 4.29, in which the distribution is dislocated from the origin $(0, 0)$. For the U_t =1.5 MV simulation, tails can be seen around the $x = 0$ line for U_e = 12.5kV. The corresponding ellipse parameters can be seen in tables 4.6 and 4.7. Comparing the results for U_t =1.5 and 2.5 MV, a decrease of R_1 of 75%, for U_e =10 kV. For R_2 a 70% decrease is found, and in θ a decrease of 9%. Consequently this results in a decrease in ϵ, by a factor of $\sim$7.8. For U_e =12.5 kV a increase in R_1 of 5% is found whereas a factor of $\sim$7 decrease in R_2 is found, the increase in angle appears to be 40%. ϵ at the end of the acceleration column decreases by 6 times. For U_e = 15kV the R_1 value increases by $\sim$9 times while the value for R_2 decreases by 17 times, the angle decreases from 2.22 rad to 1.83 rad, corresponding to a decrease of $\sim$18%. ϵ decreases by a factor of $\sim$18.

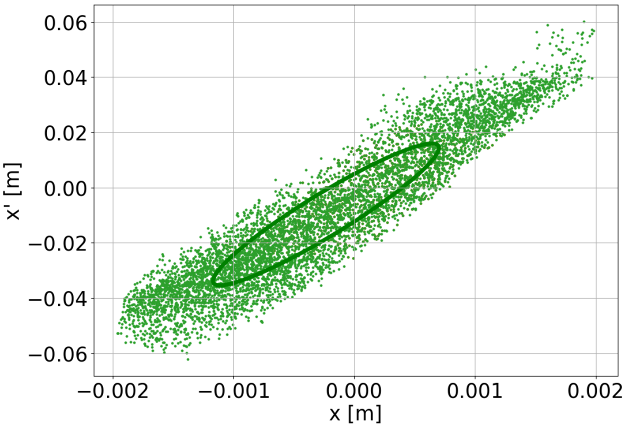

Figure 4.26: Phase space at the end of the extraction region (z=0.02 m) for the full simulation. The same result is obtained for all values of U_t and U_e.

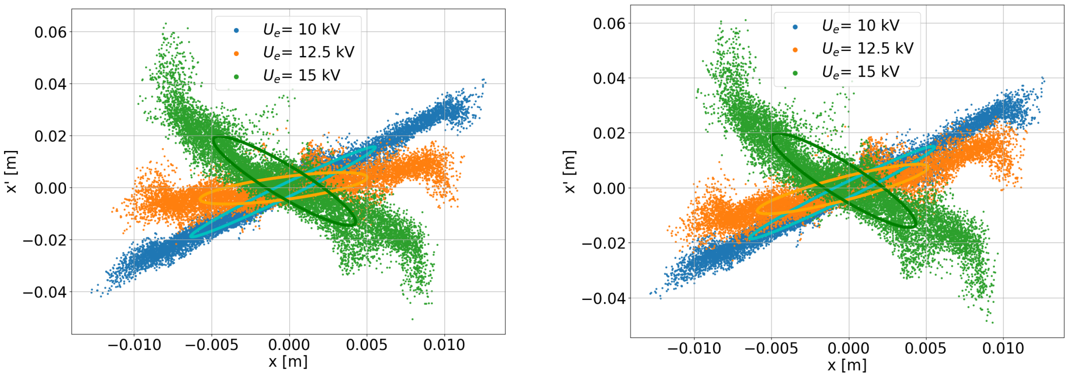

(a) U_t=1.5 MV

(b) U_t=2.5 MV

Figure 4.27: Phase space plot at the end of the Einzel lens (z=0.19 m), for the full simulation of the LIBAF Pelletron.

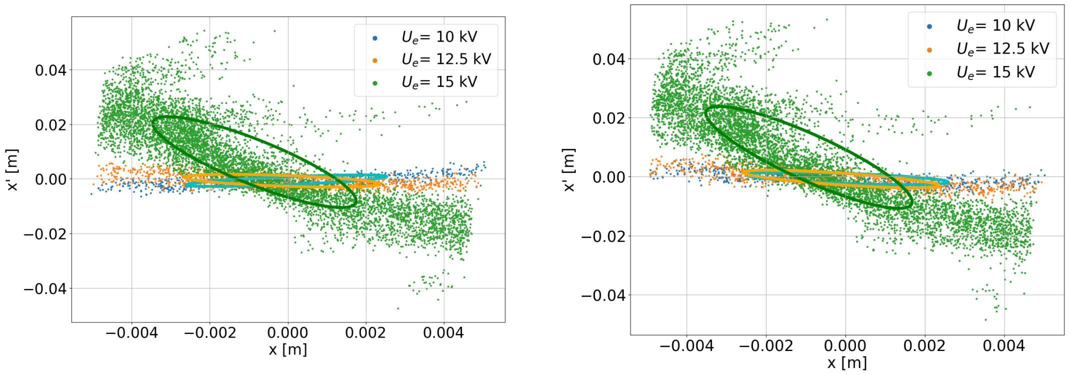

(a) U_t=1.5 MV

(b) U_t=2.5 MV

Figure 4.28: The phase spaces just after the aperture (z=0.30 m), for the full simulation of the LIBAF Pelletron.

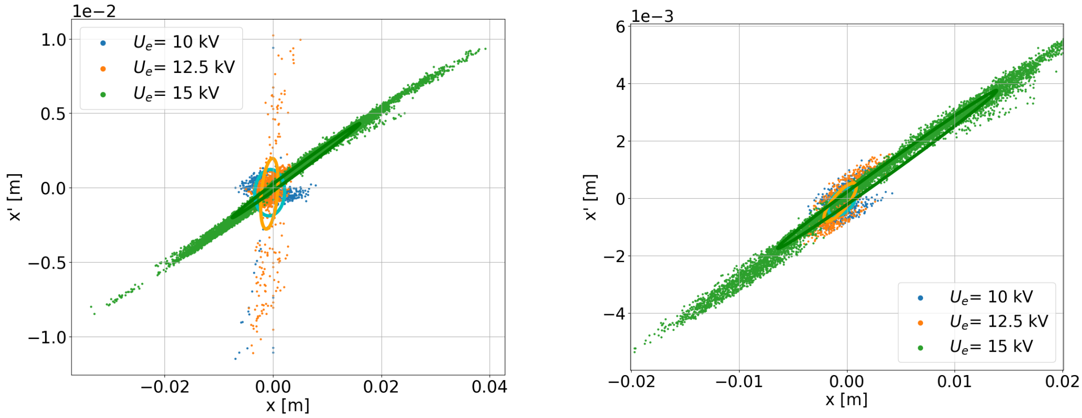

(a) U_t=1.5 MV

(b) U_t=2.5 MV

Figure 4.29: Phase space at the end of the acceleration column (z=3.68 m), for the full simulation of the LIBAF Pelletron.

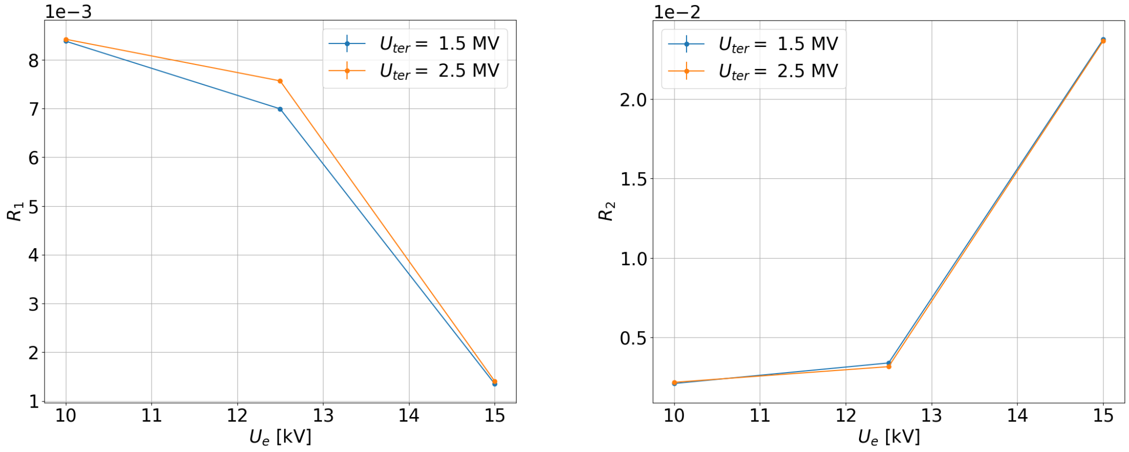

(a) R_1 **(b)** R_2

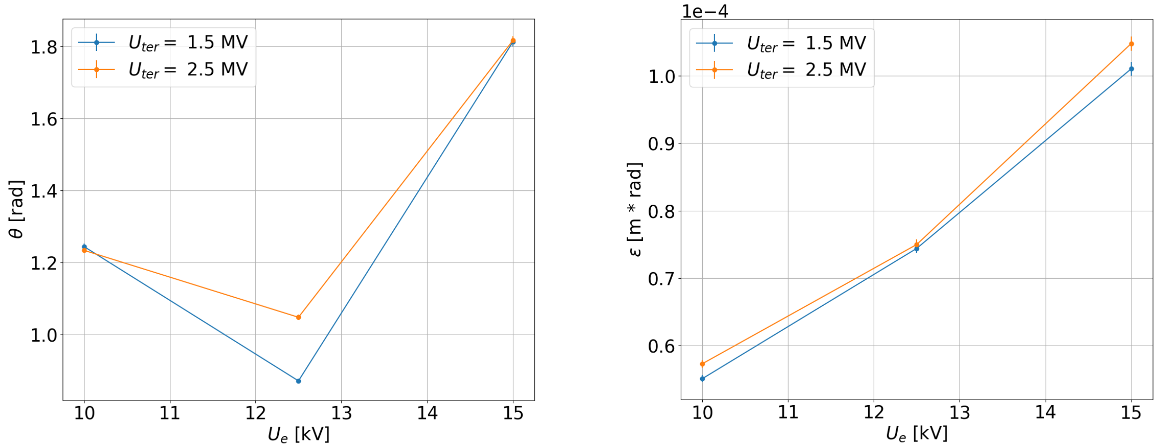

(c) θ **(d)** ϵ

Figure 4.30: Ellipse parameters of the phase spaces after the Einzel lens, at different U_e, for the full simulation. Lines are shown to guide the eye. Statistical uncertainties are indicated.

4.3.4 APR

Particle data in z was filtered to extract the number of particles that pass the slit, as is discussed in Section 3.6. The APR's are shown in Table 4.8 for both U_t =1.5 and 2.5 MV at different values of U_e. For U_e=10 kV an APR of 0.06 was found compared to a APR of 0.058 for the U_t =2.5MV, which correspond to a variation of 3%. For the U_e =12.5 kV case the variation is 15% and for the 15kV it corresponds to a variation of 7%.

Table 4.6: Fitted ellipse parameters of the phase spaces predicted at selected locations in the full accelerator simulation, for three Einzel lens potentials, with a terminal potential of 1.5 MV.

U_e [kV]	z [m]	R_1 [$\sqrt{mm^2+1}$]]	R_2 [$\sqrt{mm^2+1}$]]	θ [rad]	ϵ [μm]
10.0	0.02	1.40 ± 0.01	6.60 ± 0.05	1.54 ± 0.01	29.00 ± 0.29
	0.19	8.40 ± 0.06	2.10 ± 0.01	1.24 ± 0.01	55.10 ± 0.54
	0.30	3.40 ± 0.02	1.10 ± 0.01	2.49 ± 0.02	17.80 ± 0.18
	3.68	2.80 ± 0.02	1.50 ± 0.01	1.61 ± 0.01	13.50 ± 0.13
12.5	0.02	1.40 ± 0.01	6.60 ± 0.05	1.54 ± 0.01	29.00 ± 0.29
	0.19	7.00 ± 0.05	3.40 ± 0.02	0.87 ± 0.01	74.40 ± 0.74
	0.30	1.70 ± 0.01	2.90 ± 0.02	2.43 ± 0.02	15.50 ± 0.15
	3.68	1.90 ± 0.01	1.90 ± 0.01	1.20 ± 0.01	11.20 ± 0.11
15.0	0.02	1.40 ± 0.01	6.60 ± 0.05	1.54 ± 0.01	29.00 ± 0.29
	0.19	1.40 ± 0.01	23.80 ± 0.17	1.81 ± 0.01	100.00 ± 1.00
	0.30	1.00 ± 0.01	23.00 ± 0.16	1.70 ± 0.01	71.50 ± 0.71
	3.68	1.55 ± 0.01	2.70 ± 0.02	2.22 ± 1.92	130.00 ± 1.29

Table 4.7: Fitted ellipse parameters of the phase spaces predicted at selected locations in the full accelerator simulation, for three Einzel lens potentials, with a terminal potential of 2.5 MV.

U_e [kV]	z [m]	R_1 [$\sqrt{mm^2+1}$]]	R_2 [$\sqrt{mm^2+1}$]]	θ [rad]	ϵ [μm]
10.0	0.02	1.40 ± 0.01	6.60 ± 0.05	1.54 ± 0.01	29.00 ± 0.29
	0.19	8.40 ± 0.06	2.20 ± 0.02	1.23 ± 0.01	57.00 ± 0.56
	0.30	1.60 ± 0.01	2.60 ± 0.02	2.52 ± 0.02	14.00 ± 0.14
	3.68	1.60 ± 0.01	0.35 ± < 0.01	1.76 ± 0.02	1.72 ± 0.02
12.5	0.02	1.40 ± 0.01	6.60 ± 0.05	1.54 ± 0.01	29.00 ± 0.29
	0.19	7.60 ± 0.05	3.20 ± 0.02	1.05 ± 0.01	75.00 ± 0.29
	0.30	1.20 ± 0.01	4.00 ± 0.03	2.23 ± 0.01	15.00 ± 0.68
	3.68	2.00 ± 0.01	0.29 ± 0.02	1.93 ± 0.01	1.84 ± 0.02
15.0	0.02	1.40 ± 0.01	6.60 ± 0.05	1.54 ± 0.01	29.00 ± 0.29
	0.19	1.40 ± 0.01	23.70 ± 0.17	1.82 ± 0.01	100.00 ± 1
	0.30	0.94 ± 0.01	2.37 ± 0.02	1.70 ± 0.01	69.00 ± 0.68
	3.68	14.30 ± 0.10	0.16 ± < 0.01	1.83 ± 0.01	7.42 ± 0.07

Table 4.8: The fraction of particles that reach the end of the accelerator, at selected values of U_e and U_t, for the full simulation of the LIBAF Pelletron. Statistical uncertainties are given, based on total of 10000 particles simulated.

U_e	APR for U_t=1.5 MV	APR for U_t=2.5 MV
10.0 kV	0.060 ± 0.002	0.058 ± 0.002
12.5 kV	0.100 ± 0.003	0.085 ± 0.003
15.0 kV	0.640 ± 0.005	0.594 ± 0.005

5 Discussion

5.1 Comparison of Simulation Codes

Comparing and contrasting the simulations by the different software was performed in general test simulations for WARP, COMSOL and TRANSPORT/TURTLE by using the lattice solver and 3D solver. The results obtained from these simulations show variations between the software packages causes by the different procedures and routines on which these software packages were built. In the lattice test simulations, detailed in Section 4.1.2, large variations were found between TRANSPORT, COMSOL and WARP. These variations are clearly observed from the beam envelopes and phase spaces for each package, presented in Figure 4.2 and Figure 4.3 and Table 4.2. This results from the lattice, not taking into account the electric fields generated by the geometry [52, 55]. An example of these field regions are shown in Figure 4.4. TRANSPORT/TURTLE simulations can only be performed with the matrix representation and limited elements are available. Due to these limitations TRANSPORT/TURTLE were not used for the full simulation of the LIBAF pelletron.

In comparison to the lattice simulations, the 3D geometry simulations for WARP and COMSOL as discussed in Section 4.1.3 show variations in the envelope at z =1 m of ∼10%, as presented in Figure 4.5 and a good agreement is found in the phase spaces of WARP and COMSOL in Figure 4.6. At the end of the simulation ϵ differs by <1% and R_1 of 5% and R_2 of 6%. This significant variation of ∼6% seen in the phase space parameters R_1 and R_2 might be caused by the relatively low cell distribution used in WARP and the difference in geometry used in WARP and COMSOL which is discussed in Section 3.4.4. The angle and ϵ reported in Table 4.3 predicted by WARP and COMSOL differ by only by 3% and $< 1\%$ respectively, showing a good agreement.

The Beam Energy Study, of which results are presented in Section 4.1.4, shows how the three software packages perform at different E_0, ranging from 30-4800 kV. Investigation indicates that in the lower energy regime, at 30 kV the variation in divergence was a factor of two, seen in Figure 4.8. The point at which $f = \infty$, is found to be between 95-105 kV accelerating potential for WARP and COMSOL. The $f = \infty$ point for TURTLE was found to be ∼120 kV, a difference of around ∼15 % compared to WARP and COMSOL. This may imply that the results for TURTLE are less accurate in the lower energy regime (30-200 kV), however, no relevant literature was found to substantiate this. To the contrary, articles presenting successful simulation of accelerators in the lower energy regime for TRANSPORT/TURTLE were found [58]. Another implication could be that both WARP and COMSOL are not suitable for the modelling of low energy ion beam, however, this is less plausible.

The mesh convergence study, presented in Section 4.2.1 shows the effect of the mesh on the geometry (figures 4.12 and 4.11), phase ellipses (Figure 4.14) and envelopes (Figure 4.13). Visually large difference can be seen in the mesh projection on the geometry, shown in Figure 4.12, for WARP and COMSOL at a normal mesh and cell division of 75|75|100 respectively sharp edges are introduced in the meshed geometry, these edges can introduce artifacts and non-physical effects on the fields that are resolved on the mesh. For the meshing in COMSOL almost no variation is seen in the envelope of the acceleration column, seen in Figure 4.13 at different mesh granularities. On account that almost no variation is seen in COMSOL, that may be caused by the fact that only standard physics defined mesh granularities were used as discussed in Section 3.5.1. Large differences are observed for WARP at different cell divisions, and therefore, increasing the mesh enhances the accuracy of the results, however this is limited by memory usage. Memory problems occurred for COMSOL and WARP using a mesh granularity and cell division of Extremely Fine and |800|800|800 respectively, with the DESKTOP hardware used as discussed in Section 3.1.4. The simulation times in WARP were much longer, as can be seen in Table 4.4, >25 times for the smallest three granularities/cell divisions than for COMSOL. This is caused by the injection scheme of the software, discussed in Section 3.5.1, where at every time step $1e4$ particles are injected causing much longer simulation times. An interesting effect is observed for the ϵ at the different mesh sizes and granularities, as can be seen in Figure 4.14, the ϵ remains constant within statistical uncertainty for WARP, however for COMSOL a convergence is observed by increasing the mesh granularity from normal to extra fine with a decrease in ϵ of $\sim$ 30%. The highest mesh was used for the acceleration column.

5.2 Ion-source and Extraction

The beam input used for the simulations is described in Section 3.3, simulations were run to validate that the beam input is the same for all software. Results of these simulations are presented in Section 4.1.1, in Table 4.1 the phase space parameters were found to be within 3%. The results presented in this work assume a mono-chromatic beam, as discussed in Section 3.1.2, however, a real beam always has a finite energy distribution. Accelerator systems are design and optimized to create a beam with a well defined energy and small energy spread to allow a high resolution as a micro-probe. The ion source, discussed in Section 3.5.3 is modelled according to specifications given by the NEC brochure [56]. It is unknown if these parameters give an accurate representation of the actual beam emitting from the ion source.

Simulations of the LIBAF Pelletron in COMSOL show no significant variance for the selection of U_e in the extraction section of the accelerator at U_t =1.5 and 2.5-MV as is seen in Figure 4.26 and tables 4.6 and 4.7. The resulting phase spaces and envelopes, seen in figures 4.24 and 4.25 only show variation within the statistical uncertainty. It is therefore concluded that the extraction is independent of the values of U_t and U_e.

5.3 Einzel Lens

It can be seen in Figure 4.30 that the focusing effect of the Einzel lens is dependent on U_e and independent of U_t for the 10 and 15 KV Einzel potentials within variation corresponding to the literature discussed in 2.2.4. At U_e =12.5 kV, however, a variation is seen which may be caused by fields entering the Einzel lens region, further work is needed to substantiate this. The envelopes of the Einzel lens, shown in Figure 4.19 show that the focusing effect seem to be very similar for WARP and COMSOL, showing comparable envelopes at the selection of U_e. The variations found in WARP may be caused by the relatively small amount of particles that are used in the simulation N=1e3 compared to N=1e4 in COMSOL (discussed in Section 3.5.3). A good agreement between COMSOL and WARP is found for the $f = \infty$

point of the Einzel lens, which can be seen in Figure 4.22. The $f = \infty$ point was found to be between 12.7 - 12.8 kV, which is an important parameter for creating a low ϵ ion beams. The divergence as a function of U_e also shows good agreement between COMSOL and WARP. An ϵ growth is observed in Figure 4.22 for both WARP and COMSOL as U_e increases. The comparative study for the full simulation on the phase spaces, seen in figures 4.27 and 4.27 at different U_e show variations of less than 1% in R_1 for U_t =10 kV and 12.5 kV, while large deviations are found in the R_2 values between 10-30%.

The "noodle effect" [59], describing tailing particles with large variations in x' forming a HALO can be observed in the phase plots for the Einzel lens and full LIBAF simulation in Figure 4.20 and Figure 4.27 respectively. The effect is enhanced for higher U_e and in the case of the full simulation the tails have a different shape and are not symmetric in x. It is presumed that the "noodle effect" is the result of non-linear forces acting on the beam. This is supported by literature, where non-linear effects, e.g. caused by the space charge force show the same effect on the phase space distributions of particles [60, 61, 62]

The exclusion of space charge effects in all simulations were justified by the space charge effects study described in Section 3.4.6, for which results are presented in Section 4.1.5. The self-potential of the beam can be observed in Figure 4.9, showing a large potential (>45 kV) in the center of the beam that is reduced as the beam propagates and diverges, causing the space charge effect to get smaller. A point of interest is the beam potential distribution at the start (z=0) where the potential does not seem to be maximum, which is not expected. Furthermore, from the results seen in Figure 4.10, it was established that up to a current of 1 mA (K =1.25e-4) the resulting deviations were less than 4% over the region of z =0.8 m. The practical current in the LIBAF Pelletron is estimated to be around 0.1 mA and therefore, using extrapolation, a increase in beam width of 0.1% is estimated which is insignificant.

5.4 Velocity Selector

The physical principle of the velocity selector was validated by proof of principle simulations, results show that the velocity selector can be used to filter particles based on the initial energy and the electric and magnetic field ratio, this corresponds to the theory discussed in Section 2.2.3. For the monochromatic been it has been found that the response of the velocity selector is the same for an input beam as it is for a pencil beam where in both cases a deviation of 7.5 mm was observed over z =0.5 m for a $E_f = 2E_0$ =100 keV. The geometry of the velocity selector in the LIBAF Pelletron was not incorporated into the full simulation, which might cause deviation in results compared to the practical situation.

The proof of principle simulations, results of which are presented in Section 4.2.2, show the effects of the velocity selector on the beam. The envelopes and phase spaces, seen respectively in figures 4.18 and 4.17 show that the beam is displaced by the velocity selector according to the forces indicated in the figure. For a filtered energy of $2E_0$ a displacement of 7.5mm was found. The displacement of the beam is in the direction of the defined magnetic and electric field and therefore, have a effect on only one dimension of the beam. Hence, for further work, the x and y planes cannot be treated symmetric and the envelopes cannot just be expressed by $r^2 = x^2 + y^2$ as is discussed in Section 3.5.2.

5.5 Acceleration Column

For the simulation of the acceleration column, results of which are presented in sections 4.2.1 and 4.3, focusing of the beam by the fields can be observed according, to the theory discussed in Section 2.2.1, for COMSOL, WARP and TURTLE. In Figure 4.15 it can be observed that the envelopes are similar and good agreement (within 10%). On the other hand, the phase space seen in Figure 4.16 and the parameters summarized in Table 4.5, vary by 30% in R_1 and R_2. In addition, ϵ varies by 16% between COMSOL and 20-30% for TURTLE or WARP and COMSOL. The variation between COMSOL or WARP and TURTLE is partially caused by the matrix formalism which utilizes the thin lens approximation, other variations are induced by slight differences in geometry and segmentation of the elements. The segmentation is the subdivision of the elements to and is key to the accuracy of the simulations in TRANSPORT/TURTLE [58, 63]. The 3D rendering of the geometry and the beam propagation can be seen in Figure 4.23. The beam is extracted by the extraction plate and propagated through the Einzel lens where a focusing effect is observed, at the aperture the beam is cut and is accelerated through the acceleration column focusing the beam, finally reaching the accelerator exit with a small profile.

5.6 Properties of the Beam Exiting the Machine

Simulations of the LIBAF Pelletron clearly show that the combination of U_t and U_e govern the beam characteristics at the end of the accelerator, which can be seen in tables 4.6 and 4.7 and figures 4.24 and 4.25. The trailing particles previously observed in the Einzel lens and aperture ellipse can still be seen in Figure 4.29(a). Particles are lost by the aperture that is located after the velocity selector, the APRs are reported in Table 4.8. At U_e =15 kV and U_t =1.5 MV, the focal point of the beam is located directly behind the slit, focusing the majority of the particles through the slit (APR=0.640), however, a relatively large ϵ of 130.00 μm is observed at the end of the acceleration column. For U_e = 12.5 kV the focal point is located much further causing decrease in ϵ to 11.20 μm at the end, yet an APR of 0.100 is reported. Decreasing U_e to 10 kV causes a near parallel beam, however an increase of ϵ to 13.50 μm is observed and only 6% of the particles make it to the end (APR=0.060). Increasing U_t = to 2.5 MV causes an emittance decrease to 1.72 μm for U_e =10kV, at this U_t and U_e an APR of 0.058 is found which is an reduction of 5%. Increasing U_e to 12.5 kV causes ϵ to increase to 1.84 μm and an APR of 0.65, an reduction of 18%. At 15kV the majority of particles, $\sim$ 60% (APR=0.594) make it to the end at with ϵ of 7.42 μm. Generally, it can be concluded that the emittance at the end of the accelerator and the APR are governed by U_t and U_e. An emittance growth at the end of the accelerator is seen for $U_e > 10$ kV in both WARP and COMSOL. The APR's summarized in Table 4.8, reported for three settings of U_e and two selections of U_e, give a direct insight into the maximum current that can be extracted from the accelerator. This is very important parameter for the new neutron production beam line at LIBAF as the neutron production is proportional to the supplied proton beam current [1, 2].

5.7 Additional Considerations

One of the major assumptions used in the simulation is that of the perfect vacuum. This is physically unrealistic and is not accounted for, while the pressure in the machine is especially low (5e-9 mbar) interaction with the background gas still occurs and has an effect on beam broadening.

Investigation of the uncertainties caused by the component geometry tolerances is also required and must be incorporated. Especially because at some point in the time the support bars for the acceleration column were replaced. This in turn has caused a significant miss alignment at the accelerator exit. Misalignment can be modelled by taking additional parameters into account.

Although simulations presented in this work might give more insight into the processes and principles that govern the operation of the accelerator, the simulations have to be compared to measurement to asses the validity and operation range. Simulations have been cross compared by other packages and validation by measurement is still missing, future work may provide answers to the variations that are seen in the simulations.

One of the systematic uncertainties induced by WARP in the results of the phase spaces are due to particle selection discussed in Section 3.2.4. In COMSOL, particle data is extracted at a certain time step corresponding to a z position of the particles. This method created systematic uncertainties in the results that have large effects on the comparison and validation of the software. In TURTLE, deviations in results may be induced from the fact that the energy has to be changed to some discrete or rounded value in some files to be able to run the simulations, the causes of this are unknown. Envelopes of the simulations with a Gaussian beam, also discussed in Section 3.2.4 are created by extracting the r and z particle data and binning those data, the data is extracted for a finite amount of timesteps. The amount of timesteps at which the data is extracted causes a systematic uncertainty in the z data.

6 Conclusions

In this work simulations of the LIBAF pelletron were performed, in three software packages: COMSOL, WARP and TURTLE/TRANSPORT. The goals of the project were: to compare the simulation codes, to model the individual accelerator components and to incorporate the individual accelerator components into a full source-to-exit simulation. Cross-validation of the software packages was performed by test-case simulations and variations observed between the three packages were discussed. Greater insight into the parameters governing the LIBAF accelerator was gained through the individual component simulations, results indicating the trends of, and relations between these parameters. These findings have been discussed in the context of the full accelerator simulation and beam parameters at the exit of the LIBAF Pelletron were predicted. A summary of the key findings of this work is presented in Section 6.1. Recommendations for future work are presented in Section 6.2 and the closing remarks are given in Section 6.3.

6.1 Summary of Key Findings

A list of the key findings related to the comparison of simulation codes:

- A ~30% variation was seen between the envelopes, predicted by TRANSPORT and WARP, at the end a 0.5 m drift and 0.5 m acceleration when applying the lattice solver.
- WARP and COMSOL show a good agreement in 3D test simulations, with values of ϵ differing by <1% and r <10%.
- A 2x variation was found between the divergences predicted by TURTLE and the other two packages at E_0 =30 keV, for the 3D test geometry simulation. Good agreement is found in this regime between COMSOL and WARP. At higher energies (>200 kV), WARP and COMSOL results begin to diverge.
- The accelerating potential in the 3D test simulations, which results in a focal point of $f = \infty$, lies within the region 95-105 kV for WARP and COMSOL, where as for TURTLE was found to be ~120 kV.
- The mesh convergence study showed no significant effect on the beam envelopes of COMSOL. However, a variation in ϵ of ~30% was seen. For WARP significant effects on the beam envelope were observed, although ϵ remained constant.

A list of the key findings related to simulation of the individual LIBAF Pelletron components:

- Good agreement was seen in the envelopes and focal points for the Einzel lens, in WARP and COMSOL. $f = \infty$ is obtained at between U_e =12.7 and 12.8 kV, for both packages.

- The "noodle effect" is obeserved in both WARP and COMSOL causing an emittance growth for increasing $U_e > 10$kV at the end of the Einzel lens.
- A 30% variation was found in R_1 and R_2 of the phase space ellipse between WARP and COMSOL for the simulation of the acceleration column.

A list of the key findings related to the incorporation of the components into a full source-to-exit simulation of the LIBAF Pelletron:

- A study on the space charge effects substantiated the exclusion of these effects in the simulation for currents below 100 µA, which effects are estimated to be less than 1%.
- An effect of U_t on the focal point of the Einzel lens is seen for U_e=12.5 kV.
- The emittance of the beam exiting the machine is proportional to the APR which corresponds to the maximum attainable beam current which can be extracted from the machine
- The envelope and phase space results for the extraction are identical (<0.01%) and thus, independent of U_e and U_t in the modelled range.

6.2 Recommendations for Future Work

Recommendations for future work are presented:

- Validation by measurement of the simulations performed in this study to asses validity and operating range.
- Usage of other software and simulation packages, further strengthening the cross-validation. SIMION is an commercial software package widely used for similair applications, using FDM. Also recommended to take a look at TRACE-3D [64] and other software provided by accelsoft [65]. IBSIMU is also a package that seems suitable for this application [66].
- A more concise way of extracting the data in both WARP and COMSOL to limit the systematic uncertainties that are caused in this way. It is recommended to use intercept planes in x, y to extract the moments of the particles as they pass through these planes.
- Extension of the beam energy study in a larger range of energies and compare qualitatively to literature. Substantiate the validity of software packages in the lower or higher energy range.
- Further study of the non-linearities seen in the focusing of the Einzel lens to attain knowledge about possible ways to suppress these non-linear effects. Non linear effects are in most cases undesirable.
- An in depth study of the effects of the U_t on the Einzel lens focusing preceding the accelerating column, one of the results presented shows that the focusing changes for the $U_t = 1.5$MV compared to U_t =2.5 MV case which is not expected. This study can be performed by taking a larger range of U_t and U_t to establish if the effects occur over the whole range and at what conditions.

- Run simulations with a chromatic beam for a variety of velocity selector settings to see the filtering effect on the ion beam phase space and envelope in both x and y plane, resulting in a more realistic simulation. Additionally the geometry can be recreated from the NEC schematics to get a better representation of the real scenario and also be incorporated into the full simulation.

- Extension on the study of the full simulation by linear fitting of the envelopes to obtain the divergence and focal points at different settings.

- Full simulation of the ion source and comparing it to the beam properties described in [56] and on the results that follow the ion source.

- For further work an extension of the mesh convergence with finer and coarser meshes is recommended. Also implementing user defined and adaptive meshes, in this case better hardware is also recommended.

- Perform the space charge study for a general case and normalize the results so that they can be used as a major go to study for ion beam simulation. General studies on space charge were not found in literature.

- An extension to the study based on the maximum attainable current that can be extracted from the accelerator. Using a more diverse variety of settings for U_t and U_e, also incorporating simulations with varying probe potentials. A trend can be searched for an optimisation can be performed by using this trend to estimate neutron production rates in the neutron generation beam lines.

- A study on the effects of interaction of the proton beam with background gas to justify that these effects can be neglected in ion beam simulations.

6.3 Closing Remarks

After ten days and 130 hours I am honoured to say this work has been finished, in time. I enjoyed working on this project and getting to know more about the field of accelerator physics and modelling. I have learned a great deal from my supervisor and the people I met throughout this project, although, limited by COVID-19.

References

[1] M. Kristensson. *Characterisation of a neutron experimental station at the Lund Ion Beam Analysis Facility.* Master's thesis, Lunds Universitet, Nuclear Physics Division (2018)

[2] H. Perrey, M. Elfman, K. Fissum, *et al.* From micro- to macro- neutron sources: The Lund Broad-band Neutron Facility. *EPJ Web Conf.*, vol. 231 (2020), 01005. doi: 10.1051/epjconf/202023101005

[3] S. A. Johansson, T. B. Johansson. Analytical application of particle induced X-ray emission. *Nuclear Instruments and Methods*, vol. 137 (1976), 473–516. doi:10.1016/0029-554X(76)90470-5

[4] H.-K. Li, R. Akselsson. Rutherford Backscattering - A Tool for Quantification of the Results of PIXE Analysis of Single Hair Strands. *Nucl. Instrum. Methods Phys. Res., B*, vol. 12 (1985), 265–268. doi:10.1016/0168-583X(85)90061-8

[5] N. de La Rosa. *Investigation of lithium and fluorine content in geological materials using Nuclear Reaction Analysis (NRA).* Ph.D. thesis, Lund University (2019)

[6] M. Kokkoris. Ion Beam Analysis Techniques for non-Destructive Profiling Studies. In *Joint ICTP-IAEA Workshop on Nuclear Data for Science and Technology: Analytical Applications*, IAEA/ICTP Training Course (2010). Department of Physics National Technical University of Athens

[7] M. H. Herman. Applications of Rutherford backscattering spectrometry to refractory metal silicide characterization. *Journal of Vacuum Science & Technology B: Microelectronics Processing and Phenomena*, vol. 2 (1984), 748–755. doi:10.1116/1.582873

[8] C. R. Brundle. *Encyclopedia of materials characterization : surfaces, interfaces, thin films*, chap. NRA 1.11.4, 52. Boston (Mass.) : Butterworth-Heinemann, 1992. (1992). ISBN 0750691689 9780750691680

[9] R.J.W. Frost. Private Communication, University of Lund (2021)

[10] National Electrostatics Corp (NEC), www.pelletron.com, Middleton, United States.

[11] G. B. Lubkin. Chain of pellets transfers charge in electrostatic accelerator. *Physics Today*, vol. 24 (1971), 18–19. doi:10.1063/1.3022924

[12] D. Tecker. Longitudinal Beam Dynamics 1. In *Proc. of the CAS-CERN Accelerator School, Basics of Accelerator Physics and Technology* (2021). CERN, Webinar [Online]

[13] F. Tecker. Longitudinal Beam Dynamics 2. In *Proc. of the CAS-CERN Accelerator School, Basics of Accelerator Physics and Technology* (2021). CERN, Webinar [Online]

[14] H. Wiedemann. *Particle Accelerator Physics*, chap. 8: Particle Beams and Phase Space, 213–251. Springer, Cham, 4th ed. (2015). ISBN 978-3-319-18316-9. doi: 10.1007/978-3-319-18317-6

[15] T. Kalvas. Beam Extraction and Transport. In *Proc. of the CAS-CERN Accelerator School, Ion Sources* (2014), 537–564. doi:10.5170/CERN-2013-007.537

[16] L. Bartha. *Electrostatic Accelerators: Fundamentals and Applications*, chap. 11: Positive ion sources, 192–221. Heidelberg: Springer (2005)

[17] B. Holzer. Transverse Beam Dynamics 2. In *Proc. of the CAS-CERN Accelerator School, Basics of Accelerator Physics and Technology* (2021). CERN, Webinar [Online]

[18] F. Hinterberger. Ion optics with electrostatic lenses. In *Proc. of the CAS-CERN Accelerator School and KVI: Specialised CAS Course on Small Accelerators* (2006), 27–44. doi:10.5170/CERN-2006-012.27

[19] H. Wiedemann. *Particle Accelerator Physics, Ch 5: Particle Dynamics in Electro-Magnetic Fields*. Springer, Cham, 4th ed. (2015). ISBN 978-3-319-18316-9. doi:10.1007/978-3-319-18317-6

[20] F. J. Sacherer, T. R. Sherwood. The effect of space charge in beam transport lines. *IEEE Trans. Nucl. Sci.*, vol. 18 (1971), 1066–1067. doi:10.1109/TNS.1971.4326279

[21] K. L. Brown, F. Rothacker, D. C. Carey, F. C. Iselin. Transport: A Computer Program for Designing Charged Particle Beam Transport Systems. Tech. Rep. CERN–80-04, CERN (1973). doi:10.5170/CERN-1973-016

[22] I. M. Kapchinskij, V. V. Vladimirskij. Limitations Of Proton Beam Current In A Strong Focusing Linear Accelerator Associated With The Beam Space Charge. In *Proc. of the 2nd International Conference on High-Energy Accelerators* (1959)

[23] S. M. Lund, T. Kikuchi, R. C. Davidson. Generation of initial kinetic distributions for simulation of long-pulse charged particle beams with high space-charge intensity. *Physical Review Accelerators and Beams*, vol. 12 (2009), 114801. doi:10.1103/PhysRevSTAB.12.114801

[24] A. Einstein. On the electrodynamics of moving bodies. *Annalen Phys.*, vol. 17 (1905), 891–921. doi:10.1002/andp.200590006

[25] J. Qiang. Multi-Particle Simulation Techniques. Tech. Rep. CERN-ACC-2020-0012, CERN, Geneva (2020)

[26] S. Peng, J.-e. Chen, Z. Guo, *et al.* Study on Space Charge Compensation of Low Energy High Intensity Ion Beam in Peking University. In *Proc. of the 57th ICFA Advanced Beam Dynamics Workshop on High-Intensity and High-Brightness Hadron Beams* (2016), WEPM6Y01. doi:10.18429/JACoW-HB2016-WEPM6Y01

[27] M. Reiser. *Linear Beam Optics with Space Charge: Sections 4.1 - 4.6*, chap. 4, 163–272. John Wiley & Sons, Ltd (2008). ISBN 9783527622047. doi:10.1002/9783527622047.ch4a

[28] J. D. Larson. *Ion Optics and Beam Transport*, 278–298. Springer Berlin Heidelberg, Berlin, Heidelberg (2005). ISBN 978-3-540-27095-9. doi:10.1007/3-540-27095-7_22

[29] S. Humphries. *Principles of charged particle acceleration*, chap. 8, 165–196. John Wiley & Sons (1986). ISBN 0-471-87878-2

[30] H. Wiedemann. *Particle Accelerator Physics, Ch 5: Linear Accelerators.* Springer, Cham, 4th ed. (2015). ISBN 978-3-319-18316-9. doi:10.1007/978-3-319-18317-6

[31] E. Plies, K. Marianowski, T. Ohnweiler. The Wien Filter: History, Fundamentals And Modern Applications. *Nucl. Instrum. Methods Phys. Res., A*, vol. 645 (2011), 7–11. doi:10.1016/j.nima.2010.12.215

[32] W. Wien. Untersuchungen über die electrische Entladung in verdünnten Gasen. *Annalen der Physik*, vol. 301 (1898), 440–452. doi:10.1002/andp.18983010618

[33] D. Kuchler. Particle Sources. In *Proc. of the CAS-CERN Accelerator School, Basics of Accelerator Physics and Technology* (2021). CERN, Webinar [Online]

[34] C. B. Zotter. *Handbook of Accelerator Physics and Engineering*, chap. 2.4.7: Vlasov and Fokker-Planck Equations, 144. World Scientific, 2nd ed. (2013). doi:10.1142/8543

[35] A. Chao. Dynamical Systems, Representation of Particle Beams. Tech. Rep. CERN-ACC-2020-0012, CERN, Geneva (2020)

[36] K. Brown. *Handbook of Accelerator Physics and Engineering*, chap. 2.2.1 Single Element Optics, 71–74. World Scientific, 2nd ed. (2013). doi:10.1142/8543

[37] D. C. Carey. TURTLE with MAD input (Trace Unlimited Rays Through Lumped Elements) – A computer program for simulating charged particle beam transport systems and DECAY TURTLE including decay calculations. Tech. rep., Stanford Linear Accelerator Center (1999). doi:10.2172/753247

[38] U. C. Rohrer. Compendium of Decay Turtle Enhancements. Tech. rep., PSI (2006)

[39] K. Brown, C. Iselin. DECAY TURTLE (Trace Unlimited Rays Through Lumped Elements). Tech. rep., European Organization for Nuclear Research (1974)

[40] K. K. Gupta, J. L. Meek. A Brief History of the Beginning of the Finite Element Method. *International Journal for Numerical Methods in Engineering*, vol. 39 (1996), 3761–3774. doi:10.1002/(SICI)1097-0207(19961130)39:22<3761::AID-NME22>3.0.CO;2-5

[41] P. Šolín. *Partial Differential Equations*, chap. 1, 1–44. John Wiley & Sons, Ltd (2005). ISBN 9780471764106. doi:10.1002/0471764108.ch1

[42] J. Qiang, R. D. Ryne, S. Habib, V. Decyk. An Object-Oriented Parallel Particle-in-Cell Code for Beam Dynamics Simulation in Linear Accelerators. *Journal of Computational Physics*, vol. 163 (2000), 434–451. doi:10.1006/jcph.2000.6570

[43] J. M. Dawson. Particle simulation of plasmas. *Rev. Mod. Phys.*, vol. 55 (1983), 403–447. doi:10.1103/RevModPhys.55.403

[44] M. Dieckmann. The Particle-In-Cell Simulation Method: Concept and Limitations. In *2007 Summer College On Plasma Physics* (2007)

[45] A. L. C.K Birdsall. *Plasma Physics via Computer Simulations.* CRC Press (1991). ISBN 9781315275048. doi:10.1201/9781315275048

[46] D. Tskhakaya. *The Particle-in-Cell Method*, chap. 6, 161–189. Springer Berlin Heidelberg, Berlin, Heidelberg (2008). ISBN 978-3-540-74686-7. doi:10.1007/978-3-540-74686-7_6

[47] P. Monk, Y. Zhang. *Finite Element Methods for Maxwell's Equations*, vol. abs/1910.10069. Oxford University Press (2020)

[48] A. Cheng, D. Cheng. Heritage and early history of the boundary element method. *Engineering Analysis with Boundary Elements*, vol. 29 (2005), 268–302. doi:10.1016/j.enganabound.2004.12.001

[49] COMSOL. *Particle Tracing Module (user's guide)*. COMSOL Multiphysics, COMSOL, Inc., 100 District Avenue Burlington, MA 01803, USA, 5.4 ed. (2018)

[50] COMSOL Multiphysics® v. 5.4. www.comsol.com. COMSOL AB, Stockholm, Sweden.

[51] COMSOL. *COMSOL Multiphysics Reference Manual*, 5 ed. (2019). URL `https://doc.comsol.com/5.5/doc/com.comsol.help.comsol/COMSOL_ReferenceManual.pdf`

[52] U. C. Rohrer. Compendium Of Transport Enhancements. Tech. rep., PSI, http://aea.web.psi.ch/Urs_Rohrer/MyWeb/trancomp.htm (2006)

[53] A. Friedman, R. H. Cohen, D. P. Grote, *et al.* Computational Methods in the Warp Code Framework for Kinetic Simulations of Particle Beams and Plasmas. *IEEE Transactions on Plasma Science*, vol. 42 (2014), 1321–1334. doi:10.1109/TPS.2014.2308546

[54] J.-L. Vay, D. P. Grote, R. H. Cohen, A. Friedman. Novel methods in the Particle-In-Cell accelerator Code-Framework Warp. *Computational Science & Discovery*, vol. 5 (2012), 014019. doi:10.1088/1749-4699/5/1/014019

[55] D. P. Grote. *WARP Manual*. LLNL/LBNL (2000)

[56] NEC. *[Pos RF v1], Positive RF Ion Source* (2018). Available at https://www.pelletron.com/products/rf-positive-ion-source/

[57] NEC. *NEC Single Ended Pelletron Manual, Engineering Drawing Books*. National Electrostatics Corp. (1990)

[58] G. H. Gillespie, T. A. Brown. Optics elements for modeling electrostatic lenses and accelerator components: II. Acceleration columns. *Nuclear Instruments and Methods in Physics Research Section A: Accelerators, Spectrometers, Detectors and Associated Equipment*, vol. 427 (1999), 315–320. doi:10.1016/S0168-9002(98)01543-5

[59] J. C. Wheeler. *Cosmic Catastrophes: Exploding Stars, Black Holes, and Mapping the Universe*. Cambridge University Press, 2 ed. (2007). doi:10.1017/CBO9780511536625

[60] D. Jeon, J. Stovall, A. Aleksandrov, *et al.* Formation and mitigation of halo particles in the Spallation Neutron Source linac. *Physical Review Special Topics-accelerators and Beams - PHYS REV SPEC TOP-AC*, vol. 5 (2002), 094201. doi:10.1103/PhysRevSTAB.5.094201

[61] B. Marchetti, R. Assmann, U. Dorda, J. Zhu. Conceptual and Technical Design Aspects of Accelerators for External Injection in LWFA. *Applied Sciences*, vol. 8 (2018), 757. doi:10.3390/app8050757

[62] M. G. Minty, F. Zimmermann. *Transverse Beam Emittance Measurement and Control*, chap. 4, 99–131. Springer Berlin Heidelberg, Berlin, Heidelberg (2003). ISBN 978-3-662-08581-3. doi:10.1007/978-3-662-08581-3_4

[63] G. H. Gillespie. Private Communication, Gillespie Asscociates Inc. Email (2021)

[64] B. Hill, G. Gillespie, J. Moore. Using Trace 3-D in the Particle Beam Optics Laboratory (PBO Lab). In *Proc. of the 20th International Linear Accelerator Conference* (2000)

[65] G. G. Associates. Accelsoft Inc. California, USA, http://www.ghga.com/accelsoft/

[66] T. Kalvas, O. Tarvainen, T. Ropponen, *et al.* IBSIMU: A three-dimensional simulation software for charged particle optics. *Review of Scientific Instruments*, vol. 81 (2010), 02B703. doi:10.1063/1.3258608